Chapter 5

Towards the segmentation of voids using ultrasonic data

The morphology of voids plays a crucial role in accurately estimating the void volume fraction. However, our initially proposed data-driven methodology encountered limitations in discerning variances in void morphology. This shortfall may be attributable to the nature of the data, which is intrinsically linked to the ultrasonic testing methods employed. This chapter focuses on tackling the complexities inherent in analyzing void morphology. We advocate for the use of phased array ultrasonic data, complemented by advanced techniques for void segmentation in ultrasonic datasets. To achieve this, we introduce the application of Convolutional Neural Networks (CNNs) for data analysis, coupled with the acquisition of precise labels through X-ray Computed Tomography (XCT). This approach aims to enhance the accuracy and efficacy of void characterization in materials.

The chapter is divided into eight sections, as follows: Section 5.1 describes an introduction to the negation and uncertainty detection challenge. In Section 5.2, the problem is explained and translated into technical terms. In Section 5.3, we describe the methods. Section 5.4 shows the results obtained in the proposed approaches. In Section 5.5, we discuss the results obtained. Finally, Section 5.6 shows a conclusion of the chapter.

5.1 Introduction

The preceding chapter highlighted that none of the features within the data-driven methodology could effectively reflect the effect of different void morphologies. Consequently, the second objective of this thesis is to explore the feasibility of acquiring a three-dimensional (3D) representation of voids through ultrasonic data leveraging machine learning models. Specifically, the challenge addressed focuses on the absence of features capable of distinguishing void characteristics such as size, shape, and distribution. This chapter introduces one of the two proposed solutions aimed at enhancing the information provided by ultrasonic testing.

In the state of the art in porosity estimation 3.1 was exposed that several authors [41, 42, 43, 44] studied the porosity in composite materials using ultrasonic data. The experiments, however, were only able to examine the relationship between the void volume

and attenuation C-scan.

The phased array ultrasonic testing (PAUT) technology, as previously introduced in the section 2.2.1, was employed in this study to achieve optimal imaging. To the best of the authors' knowledge, this is the pioneering application of phased array technology in the examination of porosity within composite materials. Phased arrays offer several advantages [39, 61] , providing the flexibility to fine-tune various testing parameters. However, the utilization of PA does introduce certain challenges. Notably, certain characteristics come at a cost; for example, the resolution of the image is directly correlated with the frequency of examination. Higher frequencies yield better resolution, yet they result in shallower wave penetration.

The relationship between ultrasonic wave frequency and propagation depth poses a trade-off; smaller wavelengths offer superior resolution but are more attenuated than larger wavelengths. An additional challenge arises from the anisotropic nature of inspections using linear PA, where the resolution along the linear array axis is several times better than in the perpendicular axis. The size of the phased array is influenced by various factors, including the quantity and configuration of its components.

Certain characteristics come with a cost; for instance, the resolution of a picture is directly connected to the frequency of examination; the higher the frequency, the better the resolution. However, the ultrasonic wave's frequency and propagation depth are inversely connected; the higher the frequency, the shallower the wave travels. Small wavelengths allow for better scaling, but they are also more attenuated than bigger wavelengths, which is the physical explanation. Since the resolution in the axis of the linear array is a few times better than in the perpendicular axis, the inspections utilising linear PA are anysotropic, which presents another issue. Its size is determined, among other things, by the quantity of components and how they are used.

Segmentation is a crucial step in the imaging process, involving the creation of pixel-wise masks for each element in the picture. While typical ultrasonic monoelements, as employed in chapter 4 and usually found in the reviewed literature, face limitations in this regard, PA technology overcomes these constraints. PA allows for the segmentation of voids, although, as discussed later, certain challenges need to be addressed for optimal results.

5.2 Problem definition

The objective of evaluating void 3D data might involves two distinct tasks:

- The optimization of the ultrasonic PA inspection parameters:
  - Determining the focus law of the linear array.
  - Defining the central frequency of the array.
  - Configuring the set-up parameters, with a primary focus on the scan direction.
- The development of a segmentation process
  - Registration of the PAUT and XCT data.
  - Training of convolutional neural networks

– Evaluation of the results

5.3 Materials and Methods

5.3.1 Materials

The materials and its process were defined in section 4.3

5.3.2 Methodology

Our approach to ultrasonic image segmentation was to apply supervised machine learning. To do this, we propose the use of a CNN, whose performance is compared to thresholds at different gray-levels. The aim is to develop a pipeline where 2D images from the PA are the neural network input, whose output is a 2D segmentation of any voids that they contain. Therefore, 3D volumes are treated as a collection of 2D images. Figure 5.1 illustrates an overview of the methodology.

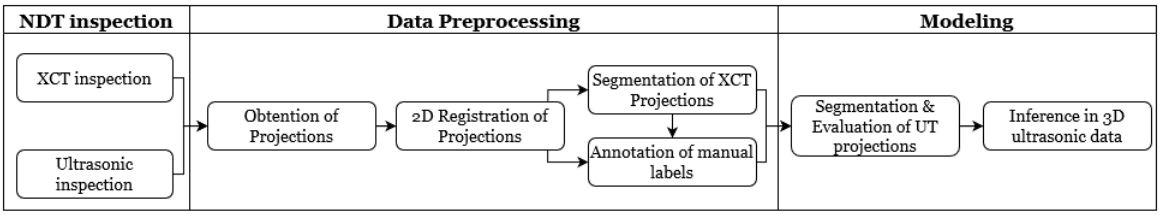

Figure 5.1: Flow diagram of the methodology.

The suggested solution is using pairs of 2D ultrasound-XCT registered projections to train a CNN. Since we only have access to the data from two coupons, we alternate between using the data from one coupon for testing and the data from the other for training. The use of XCT data and manually created labels based on the XCT and ultrasonic projections are both investigated as the ground truth. To determine how closely the neural network prediction resembles each of the ground truth sources, the model performance metrics are computed on the 2D test data set. After training, a 3D volume may be utilised to estimate porosity slice by slice using the model. An evaluation based on error measures was not possible since there were no tagged data. In order to study the variations in porosity prediction in the 3D volume, a visual comparison was done.

NDT Inspections: XCT and Ultrasonic testing optimization

To achieve accurate porosity characterization, two coupons underwent examination using X-ray Computed Tomography (XCT) with a voxel resolution of approximately 20 mum. The segmentation of voids was meticulously performed through local image thresholding in ImageJ, employing Sauvola processing techniques. This process generated a binary volume, where voids were represented by values of 1, while the substance had values of 0.

This segmented volume served as the ground truth, due to the high resolution of XCT when compared to UT.

The ultrasonic testing methodology involved an iterative approach to obtain optimal porosity images. Four ultrasonic systems were evaluated, including linear arrays with 128 elements and center frequencies of 5 MHz, 10 MHz, and 15 MHz, an 10 MHz incorporating a lens to concentrate the beam in the passive direction (perpendicular to the linear array), thus enhancing the resolution for the 10 MHz linear array. Sitau ultrasound technology (Dasel, Spain) was used, conducting examinations underwater. The array's passive direction was aligned with the longest axis of the coupons, mechanical scanning was performed along the longest coupon's axis the displacement and the displacement was recorded with an optical encoder. Pulse-echo linear scan imaging with a 32-element aperture was employed. The pitch distance between elements being 0.3 mm.

For each configuration, two parallel scans were conducted, except for the 5 MHz array, requiring manual concatenation to cover the entire width of each 40mm coupon. Rescaling of volumes was performed to maintain the component's natural ratio, resulting in a 3D volume of approximately $241 \times 120 \times 1352$ voxels in size for the final test.

Data Preprocessing

Obtention of Projection Images A 2D image registration of projections was used as the method for UT-XCT volume registration. Both volumes were manually aligned in the 3D space at a pre-processing stage. The XCT projections were obtained by summing several parallel images taken at various depths in the volume (parallel to the composite surface), whereas the US volume projections were obtained by using the maximum operator (Equation (1) defines the determination of a projection). To find enough comparable structures in the XCT and US projections, the number of photos to be included in each projection (k parameter) was manually chosen. The method is described below.

Let i = {1, . . . , l} denote the indices of the rows of a matrix A.
Let j = {1, . . . , m} denote the indices of the columns of matrix A
Let k = {1, . . . , n} denote the indices of the slices of matrix A
i,j,k are oriented to the height, width and thickness of the coupon, respectively
Let $a_{i,j,k}$ denote the value of the element A[i,j,k]
Let F be the summation in the case of XCT, and the maximum in the case of the ultrasonic data

$$\begin{aligned} &\text{projection} = U_{ij} = F(a_{ij})_{k=k_1}^{k_2}, \\ &\quad i = 1, \ldots, l \quad j = 1, \ldots, m;\ k_1 \text{ and } k_2 \text{ found experimentally.} \end{aligned} \tag{5.1}$$

The summation operation was found to be better suited for XCT because it highlights regions (white areas in Figure 5.2) and provides more microstructural information. After extracting all the images, histogram matching was applied to ultrasonic projections, and their pixel values were normalized in the interval [0,1]. This was performed to offset the differing intensity across the depth due to ultrasound wave attenuation. This methodology output a total of 12 images for two 5 mm-thick coupons. The XCT images were scaled to fit the size of the PA projections, which was equal to 470×120 pixels.

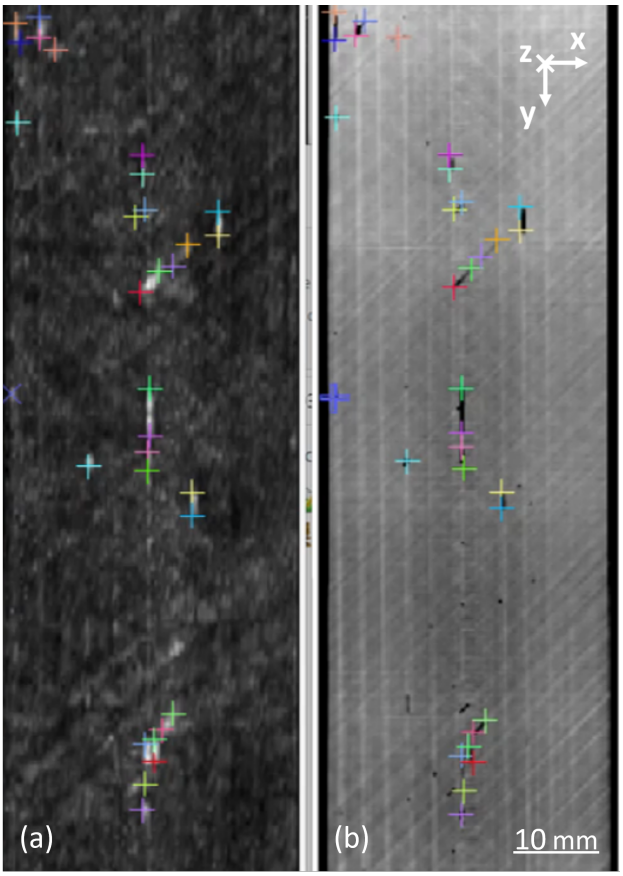

Figure 5.2: (a) UT projection of the maximum values in a slab of UT images. (b) XCT projection of the sum values in a slab of XCT images. The color crosses are the manual landmarks placed for registration.

2D Registration of Projections: The fusion of ultrasonic and X-ray computed tomography data involved a registration process for each pair of images. The ultrasonic projection served as the moving picture, while the XCT projection served as the reference. Various automatic techniques were explored, and it was observed that manually set landmarks, particularly in typical structures, yielded the most favorable outcomes, as illustrated in Figure 5.2.

The primary challenge encountered in achieving automated registration was the inability to automatically recognize equivalent keypoints in the paired images. To address this limitation, the image registration process relied on manual landmark selection. A detailed description of the image registration algorithm can be found in [91].

Labels The registration process was executed on gray-level XCT projections. The XCT-label projections were derived through the segmentation of the gray-level XCT projections. This segmentation was accomplished using the local segmentation Sauvola algorithm, implemented in ImageJ.

A second labeling procedure was necessary due to the resolution disparities between XCT and UT, as elucidated in the discussion section. For manual annotation, the registered projections of XCT and UT were superimposed, and annotations were performed based on human criteria. This approach ensured accurate alignment and annotation of the images,

taking into account the variations in resolution between the two imaging modalities.

Modeling

Segmentation of UT Projections: In the segmentation of ultrasonic testing projections, the effectiveness of a convolutional neural network (CNN) was evaluated in comparison to traditional segmentation algorithms. The following methodologies were employed and assessed:

- Global thresholds: different values for global segmentation of the projections were applied. The pixel values of the ultrasonic projections were normalized between [0,1], and the thresholds were in the range [0.25,0.4] with a 0.05 step. We also explored local segmentation algorithms such as Sauvola, but their results were found to be too noisy.
- Network architecture: the network is a slightly modified version of the one shown in [92]. The hyperparameters are shown in Table 5.1. The proposed network comprise four convolutional layers with two max-pooling layers and three FC layers. The network architecture is illustrated in Figure 5.3. It was trained from scratch using extracted patches. Convolutional layers have a 3×3 kernel, stride 1, and no padding. Max pooling is performed with a 2×2 window and stride 2. All the hidden layers, except the output units, are equipped with rectified linear units (ReLU).

Table 5.1: Table of hyperparatemers for each type of label.

Labels	Ratio	Epoch	h	s
Manual	11	20	5	1
XCT	6	25	5	1

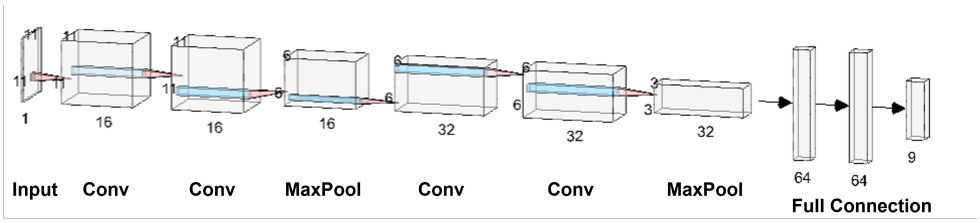

Figure 5.3: Diagram of the CNN structure. The leftmost image is the input patch with one channel. Other cubes indicate the feature maps obtained from convolution (Conv) or max pooling. All convolutional layers have a kernel of 3×3, stride 1 and zeros padding. Max pooling is performed with stride 2 over a 2×2 window.

Training and Testing In scenarios involving multiple labels, the neural network's output units are not strictly exclusive, allowing for the possibility of more than one positive output simultaneously. To effectively address this situation, the binary cross-entropy is employed as the loss function. The binary cross-entropy is defined as:

$$L = -\frac{1}{N}\sum_{i=1}^{N} y_i \log(\hat{y}_i) + (1 - y_i) \log(1 - \hat{y}_i) \tag{5.2}$$

where N is the total number of samples in the dataset, y_i is the sample's actual label (either 0 or 1), $\hat{y}_i$ is the projected probability that the sample's actual label (being a void) would fall under the positive class, and log is the natural logarithm. In the network, regularisation was not employed.

Data augmentation consisting uniquely in rotation of the training dataset was used. The dropout technique is an easy and efficient way to prevent overfitting. While training a neural network, some hidden neurons are randomly assigned a value of zero. This technique is applied to the first two fully connected (FC) layers, and the dropout ratio is set to 0.5. Weights in convolutional layers and FC layers are initialized using the Xavier method. Adam is adopted as the optimizer with a learning rate set to 0.01 and decaying to 0.002 from the ninth epoch onwards. The batch size for each iteration is set to 1256.

Evaluation As mentioned under the methodology, the evaluation was performed on a set of 2D projections (see Figure 4.8). Using this approach, it is possible to calculate precision (Pr), recall (Re), F1 score ($F1$), and intersection over union (IoU), which are defined as follows.

$$Pr = \frac{TP}{TP + FP}$$
$$Re = \frac{TP}{TP + FN}$$
$$F1 = \frac{TP}{2TP + FN + FP}$$
$$IoU = \frac{TP}{TP + FN + FP}$$

Being

- False positive (FP): negative class predicted as positive.
- True positive (TP): positive class predicted as positive.
- True negative (TN): negative class predicted as negative.
- False negative (FN): negative class predicted as positive.

5.3.3 Tools

Different open source software have been used along the project, namely TensorFlow, Fiji, Scikit-image, Jupiter Lab, Matplotlib, NumPy, Python-pillow and Napari [93, 94, 95, 96, 97, 98, 99, 100].

5.4 Results

5.4.1 Initial Phase Array optimization experiments.

The PA testing counts with several parameters that need to be optimized for a new set-up. In this case, the focus law, and the frequency of inspection were the most important.

Figure 5.4 compares the XCT ground truth to the slice of a particularly illustrative void distribution for a variety of linear arrays.

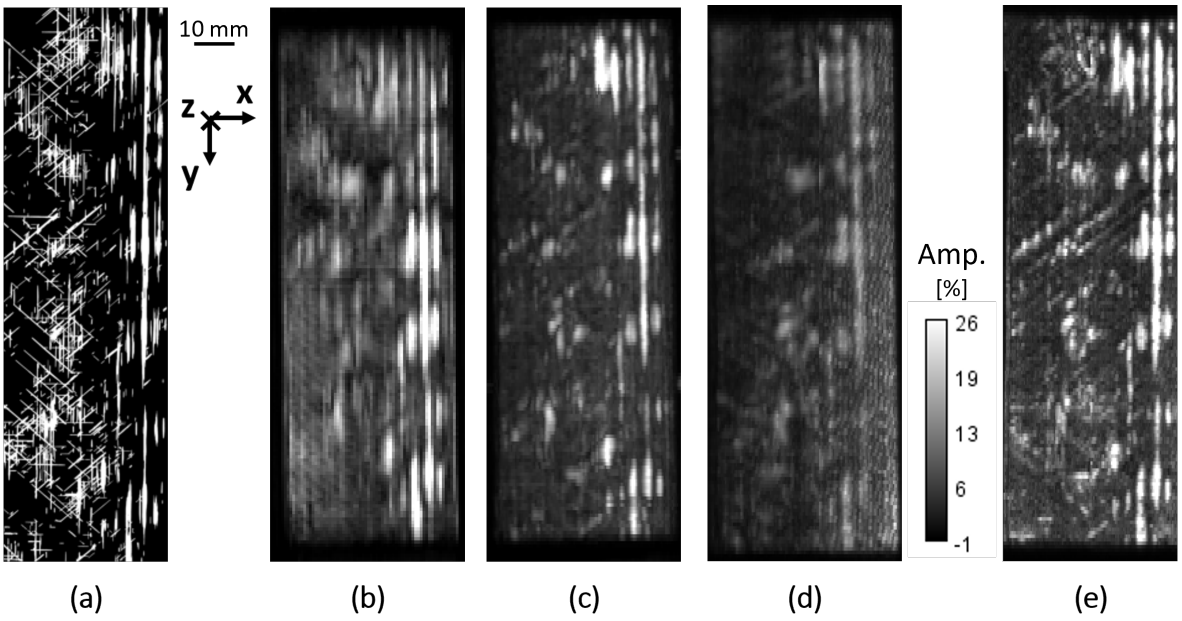

Figure 5.4: a) Projection of the segmented porosity in XCT. The phased array UT slices with central frequency equal to b) 5 MHz c) 10 MHz d) 15 MHz and e) 10 MHz and lens. The aspect ratio is not conserved. Note that the last image provides the finest detail for the voids structures, especially those oriented in ±45°

5.4.2 Dataset

Each coupon's dataset (from UT and XCT data) is made up of projections that each include a slab, or widthwise section, of the material. Seven projection pairings for Coupon 1 and five for Coupon 2 were produced due to the inherent disparities between the coupons. The process is used to produce each of the XCT/UT projections. Each projection's XY size was around 470 x 120 pixels, or about 1 mm by 2 pixels.

The dataset is displayed in figure 5.5. Each coupon's projections are arranged in order of proximity to the front surface to the rear surface. There are noticeable differences across projections in terms of the direction and size of the voids, the sharpness, and the position of noisy structures. Numerous brilliant structures in the ultrasonic data can be connected to the great majority of the voids segregated in the XCT. As a result, the preparation stage makes it possible to create a dataset for defect segmentation.

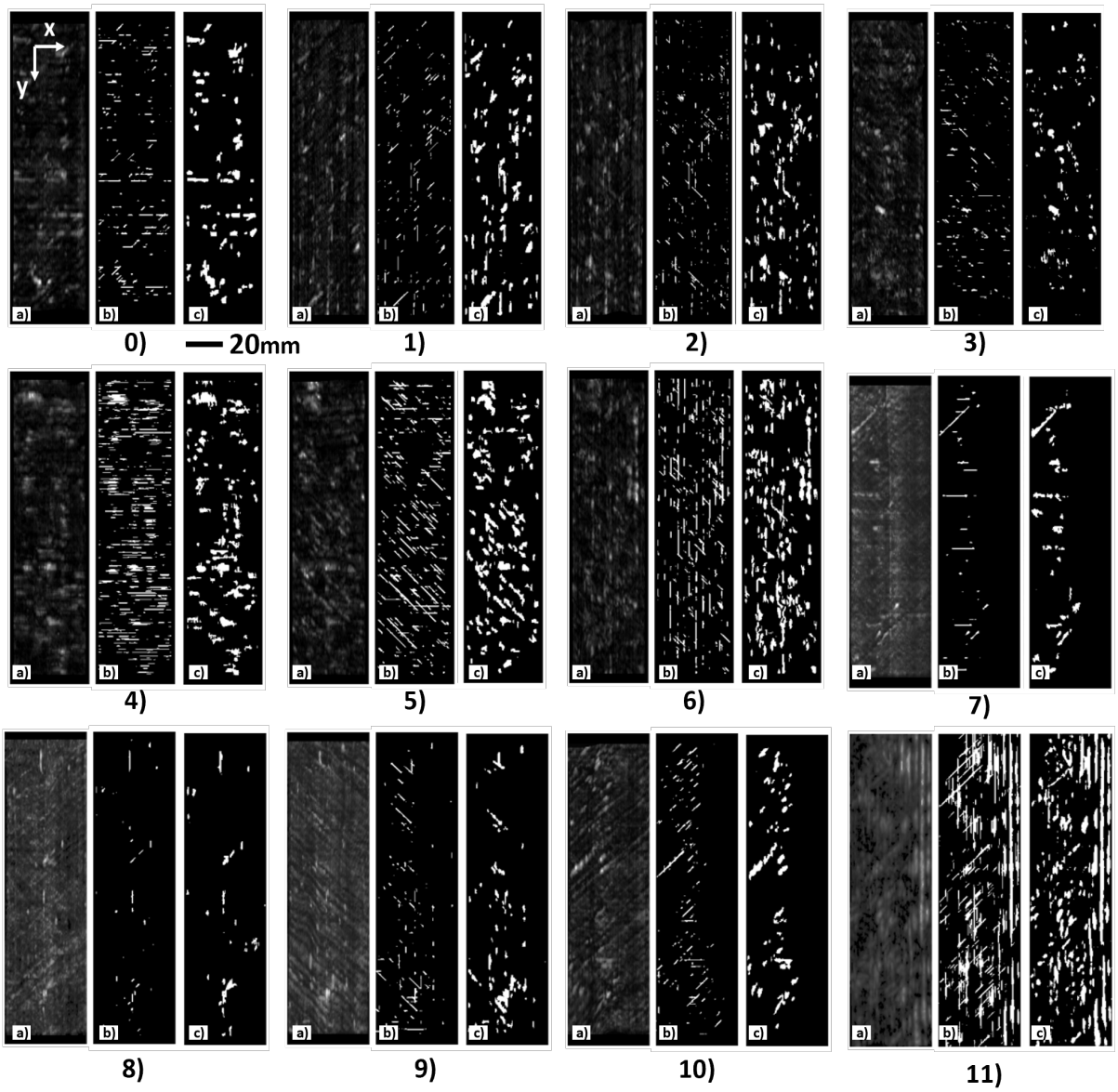

Figure 5.5: Built dataset of projections for coupon 1: [0-6], and coupon 2: [7-11]. In each triplet: a) the PAUT projection, b) XCT labels, c) Manual labels. The dataset shows a wide variety in void orientation, distribution, shape, and also in the intensity values and sharpness in the ultrasonic input, mostly linked to the scattering effect ocurring along ultrasonic wave propagation.

5.4.3 CNN Training

Given the availability of two distinct label types, the same Convolutional Neural Network (CNN) architecture was trained separately with XCT labels and manual labels. The training phase utilized the projections from one specimen, referred to as 'Coupon 1,' while the projections from another specimen, 'Coupon 2,' were used for evaluation.

Figure 5.6 showcases the CNN predictions. Specifically, Figure 5.6a depicts the ultrasonic input for the CNN trained with XCT labels, and its corresponding predictions are illustrated in Figure 5.6c. Conversely, Figure 5.6e represents the results from the CNN trained with manual labels. The validation curves for the networks, differentiated by label type, are included in Figure 5.8. Additionally, Tables 5.2 and 5.3 provide the evaluation metrics, employing projections from Coupon 1 as the training data and those from Coupon 2 as test data. Finally, Table 5.4 compiles the average evaluation metrics for all dataset projections, considering manual annotations as the ground truth.

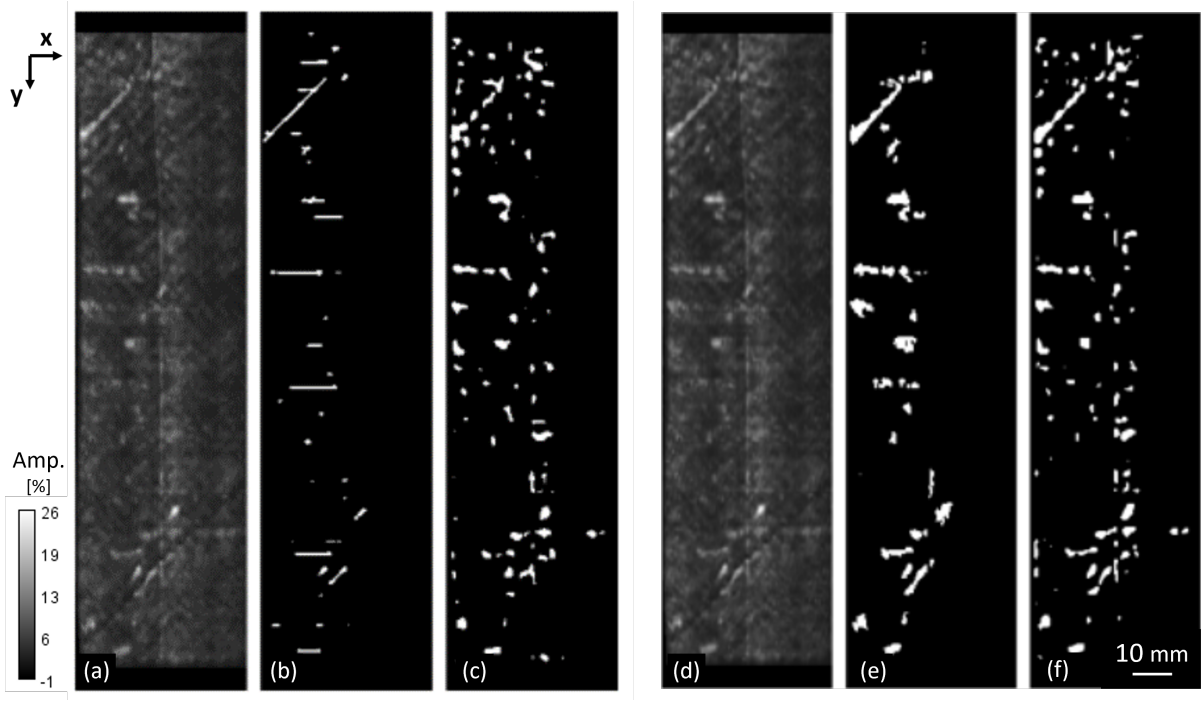

Figure 5.6: Comparative results for the first projection of test data from Coupon 2. (a) presents the ultrasonic projection input. (b) depicts the XCT-derived ground truth segmentation. (c) shows the predicted segmentation by the CNN trained with XCT labels. (d) illustrates the same ultrasonic projection input for reference. (e) displays the manual label segmentation. (f) demonstrates the predicted segmentation by the CNN trained with manual labels.

Table 5.2: Training evaluation metrics.

	XCT Labels	**Manual Labels**
Avg Training Precision:	0.29	0.90
Avg Training Recall:	0.42	0.53
Avg Training F1:	0.31	0.66
Avg IoU:	0.19	0.50

Table 5.3: Test evaluation metrics.

	XCT Labels	**Manual Labels**
Avg Test Precision:	0.27	0.67
Avg Test Recall:	0.49	0.72
Avg Test F1:	0.27	0.67
Avg IoU:	0.16	0.51

Table 5.4: Average evaluation metrics for the manually annotated labels and projections from the two coupons. In the case of the CNN, the metrics were obtained when the projections belong to the test dataset.

	avg. precision	**avg. recall**	**avg. F1**	**avg. IoU**
CNN	0.74	0.65	**0.66**	**0.50**
Thr: 0.25	0.35	**0.92**	0.44	0.30
Thr: 0.3	0.58	0.79	0.60	0.44
Thr: 0.35	0.77	0.59	0.60	0.44
Thr: 0.4	0.86	0.39	0.49	0.34
Thr: 0.45	**0.92**	0.24	0.35	0.22

Comparison of Segmentation Algorithms along the Dataset

The measured F1 evaluation metric for the segmentation results on manual labels for each threshold and the CNN are shown in Figure 5.9, the IoU in Figure 5.10.

5.5 Discussion

5.5.1 Ultrasonic testing optimization

Figure 5.4 presents the results obtained from various linear ultrasonic arrays. The 5 MHz array, as shown in Figure 5.4b, offers notable advantages, including the capacity to inspect coupons in a single scan and effectively image void structures that are aligned with the scan axis (parallel to the coupon's major axis). Its limitation, however, is the inability to detect voids at oblique angles, specifically at 0 and 45°. In contrast, the 10 MHz array

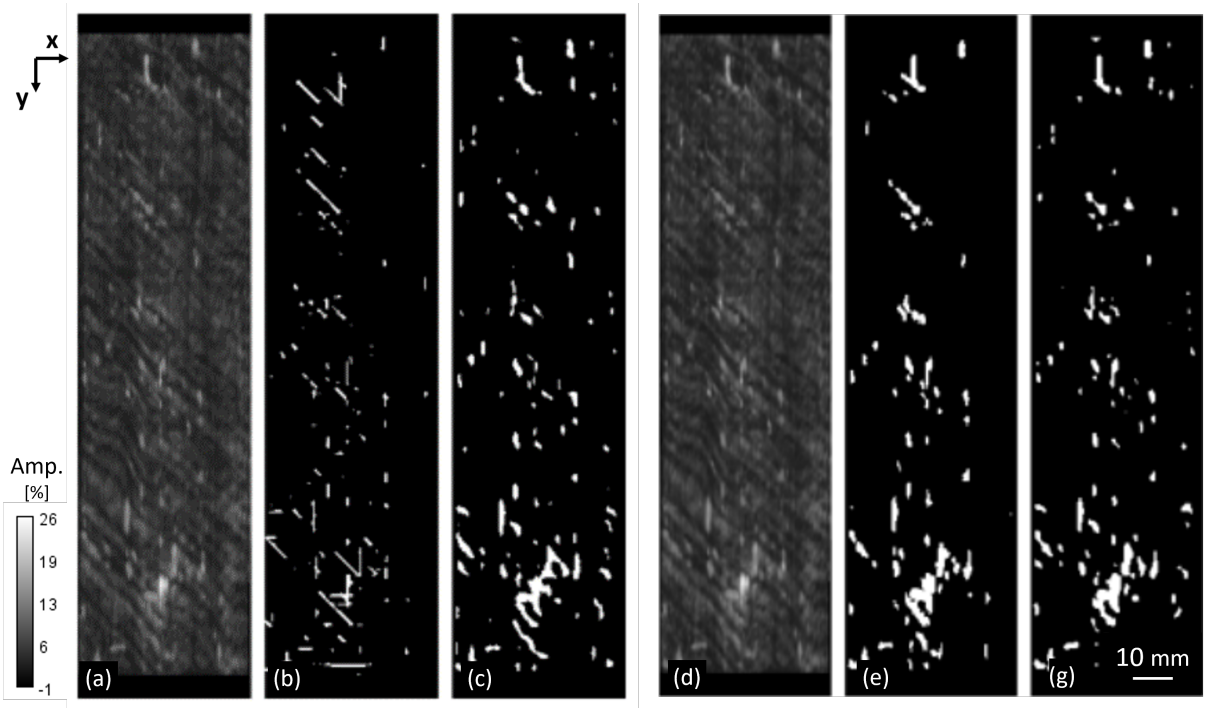

Figure 5.7: Results for the projection 3 of test data. (**a**) Ultrasonic input, XCT ground truth, and predicted image. (**b**) Ultrasonic input, manual labels, and predicted image.

(Figure 5.4c) requires two scanning scans but provides enhanced detail, particularly when voids are closely spaced, and captures structures from multiple orientations.

The 15 MHz array, depicted in Figure 5.4d, yields images with a lower signal-to-noise ratio and, in certain cases, results in signal attenuation. The 10 MHz array equipped with a lens, Figure 5.4e, emerges as the optimal solution, striking a balance by rendering voids at varying angles more discernible. It was discerned that, for the component's secondary axis, additional resolution was superfluous; however, focusing in the scanning direction (the primary axis) was beneficial, hence the incorporation of the lens.

This investigation suggests that linear arrays at 5 MHz and 10 MHz are suitable for applications where void orientation is predictable. While further research is necessary to fully ascertain the compromise between frequency and penetration depth, frequencies above 10 MHz are likely approaching their operational limit at around 5 mm depth, contingent also on the material's structure. The 10 MHz linear array with a lens proved to be the superior choice for creating the most accurate 3D representations of voids.

5.5.2 Preprocessing

The phased array amplitude C-scans enables the detection and measurement of voids down to few dozen μm thin. The human eye can establish clear correlations between void defects in XCT and C-scans. The obtention of projections was motivated as a way to deal with the mismatch in the depth dimension between the ultrasonic and XCT volumes. In this sense, the similarity in the porosity between both sources is clear. The way projections are obtained highlights the void structures, but it also strengthens echoes caused by resin areas or other structures. Although the equalization process of the ultrasonic projections

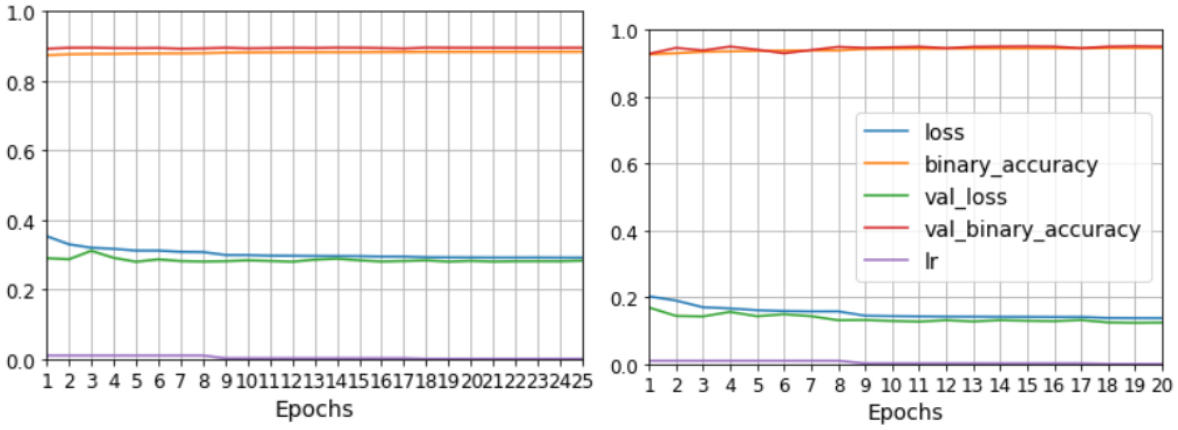

(a) (b)

Figure 5.8: Training and validation curves for the networks trained on each type of labels. (**a**) Network trained with XCT labels. (**b**) Network trained with manual labels.

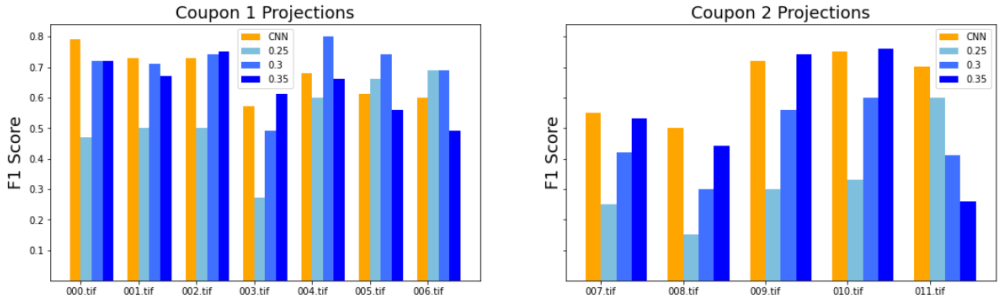

Figure 5.9: Comparison of F1 for the 0.25,0.3 and 0.35 global threshold segmentations applied to the US projection on a [0, 1] gray scale, and the CNN. In the case of the network, the value of F1 was obtained when the image formed part of the test dataset.

compensates for the attenuation along the thickness, probably other techniques, such as an adaptive time gain (TGC) during inspection, may improve the results.

5.5.3 Registration

We found that 3D registration was not accurate enough to train the CNN, mostly due to the mentioned mismatch in the depth dimension. The automation of registration is primarily limited by the difficulty in automatically detecting common salient structures, structural descriptors, or any metric of statistical dependency for both data sources. However, once the algorithm developed in [91] counts with enough common keypoints between the 2D images, registration is successful. A possible future line of research would be to explore whether deep learning models are able to find similar keypoints, for which purpose our annotated data could be used.

5.5.4 Evaluation and Labels

Two different image labels were used as ground truths in two independent training sessions. The use of XCT projections as labels is the most straightforward training method for

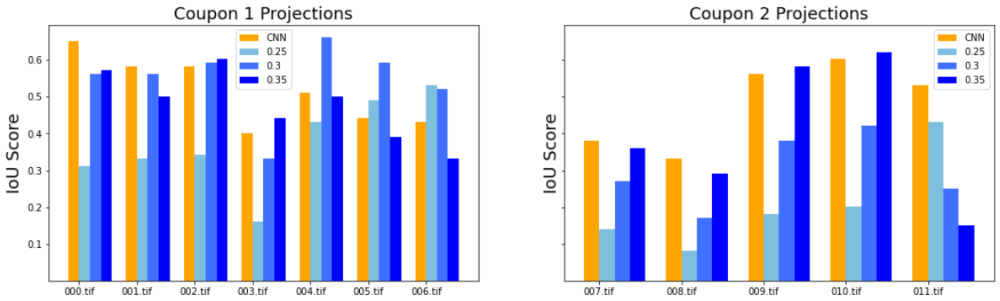

Figure 5.10: Comparison of IoU for the 0.25,0.3 and 0.35 global threshold segmentations applied to the US projection on a [0, 1] gray scale, and the CNN. In the case of the network, the value of IoU was obtained when the image formed part of the test dataset.

a CNN. However, each source has different resolutions, which results in data that are not adequate for the classification task. On this ground, we also used manual labeling. Figure 5.11 illustrates the differences in labeling porosity between the XCT projections (through automatic local thresholding) and the manual labels in US projections. Bright pixels account for internal echoes, which can be caused by defects caused by porosity or by the internal microstructure of the composite, for instance, resin pockets. The aim of the network is to segment the defect echoes. If XCT labels are used, there is only a small difference between void and nearby pixels. The different resolutions of the NDT techniques account for this behavior. Manual labeling is performed assuming that all bright pixels within a specified region should be produced by the voids. As a result of the above resolution effect, the precision, recall, and F1 results measured using the manual labels are double that of the XCT labels.

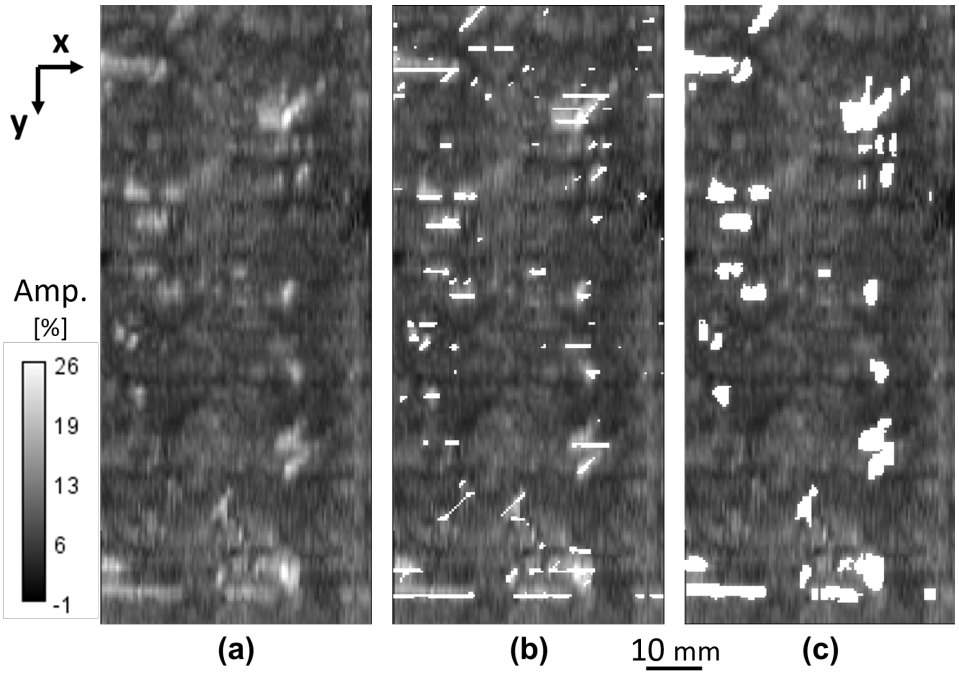

Figure 5.11: Detail of a projection illustrating the differences between the two labels used. (**a**) Ultrasonic input. (**b**) XCT labels superimposed. (**c**) Manual labels superimposed

Manual labels are the best option for training the network. However, XCT labels are still needed to perform manual labeling. In other words, the XCT ground truth is required

to single out echoes produced by defects from those produced by other factors such as microstructure or noise.

5.5.5 Segmentation Results

The evaluation metrics in Table 5.4 shows that the CNN performs better than any threshold in average for the entire dataset. F1 and IoU values of 0.66 and 0.50 respectively are insufficient for usage in a production setting. Despite this, it's not very far to production-level outcomes. The performance level may be raised to meet the criteria using techniques like those indicated in the state-of-the-art, which combine A-scan signal data with C-scans and a larger dataset. The evaluation of the models in terms of object detection metrics will still need to be done in the future.

As Figures 5.9 and 5.10 show, the performance varies in a range up to 0.2 in F1 and IoU across the different projections. The CNN fails when it comes to difficult segmentation scenarios, such as noisy projections close to the front surface, as the two initial projections in the Coupon 2 dataset and the last projection in Coupon 1 (see dataset in the appendix), or in resin-rich pocket regions. Another factor was the direction of the voids; in projections like 3 and 4, where there were more voids with a horizontal or diagonal alignment, the metrics were lower. These difficult scenarios were validated by the visual evaluation following the 3D prediction: slices of resin constructions taken close to the front or rear surfaces revealed echoes that could not be distinguished from the flaws. The improvement of the signal-to-noise ratio, deconvolution of the A-scan data, greater optimisation of ultrasonic imaging, and the incorporation of new aspects of the ultrasonic signal are potential remedies in this area of future study.

The robustness of the training is a crucial finding; test and training outcomes are same whether the CNN is trained using data from Coupon 1 or Coupon 2. In other words, the assessment measures are the same whether Coupon 1 forecasts are used for training or testing. Even when the roles of the training and test data are reversed, the network seems to be able to understand where segmentation has to be done and is reliable.

5.6 Conclusions

We created a method to use a convolutional neural network (CNN) to semi-automatically separate faults in 3D ultrasonic data. Phased-array ultrasonic testing and X-ray computed tomography data fusion make up the approach. The CNN was subsequently trained using supervised classification on 2D pictures. This method enables the measurement of evaluation criteria including accuracy, recall, F1, and IoU. The effects of applying global thresholds to the phased array and the CNN outputs were contrasted. The measures used showed that CNN performed significantly better than the worldwide benchmark.

Data fusion is one of the most difficult things to do. Since 3D registration was found to be insufficiently precise to train the CNN, an image registration mechanism for the 2D pictures produced by each approach is the suggested fix. However, registration is not entirely automated in the absence of a method to identify shared keypoints or any sort of similarity metric between the two data sources. Future research in this area may benefit

from the use of deep learning based on the manually annotated data presented here.

We investigated the use of XCT segmented voids and hand labelling as two ground truths. It was discovered that the XCT labels produced data that was too noisy for CNN training, but handwritten labels offered more reliable training. For manual labelling, the assessment metrics were twice as excellent. The network results were superior to those for the global thresholds, with an F1 for test data equal to 0.63 and an IoU equal to 0.5. CNN, however, is unable to differentiate between echoes generated by microstructural components like resin-rich regions and echoes generated by defects like porosity. Future research should enlarge the dataset, boost the signal-to-noise ratio, and incorporate more data from C-scan and ultrasonic signals. We created a method to use a convolutional neural network (CNN) to semi-automatically separate faults in 3D ultrasonic data. Phased-array ultrasonic testing and X-ray computed tomography data fusion make up the approach. The CNN was subsequently trained using supervised classification on 2D pictures. This method enables the measurement of evaluation criteria including accuracy, recall, F1, and IoU. The effects of applying global thresholds to the phased array and the CNN outputs were contrasted. The measures used showed that CNN performed significantly better than the worldwide benchmark.

Chapter 6

Classifying porosity using ultrasonic signal properties

In this chapter, we address the challenge of classificating the porosity by size and morphology distribution. In contrast with the previous chapter, the solution is adapted to work in any ultrasonic system -not necessarily phased array-. The chapter is divided into six sections, as follows: Section 6.1 introduces the the challenge that was already presented in detecting porosity size and morphology distribution using ultrasounds. In Section 6.2, we define the problem. Section 6.3 shows the experimentation and Section 6.4 shows the results obtained in the proposed approaches. In Section 6.5, we discuss the results obtained. Finally, Section 6.6 shows a conclusion of the chapter.

6.1 Introduction

This limitation prompted the exploration of a three-dimensional representation of void spaces in the previous chapter, suggesting the potential utility of precise void segmentation in ultrasound imaging. However, achieving such segmentation typically requires sophisticated phased array equipment, which excels in mitigating background noise and enhancing void classification accuracy. Nonetheless, these advanced systems are not as commonly used as traditional monoelement transducers in ultrasound inspections. Consequently, developing methodologies enabling the analysis of void characteristics using widely available monoelement transducers, could offer a more accessible alternative reducing the investment in advanced equipment and associated training.

Chapter 2.2 introduced the analytical signal concept. Several studies [13, 14, 15, 16, 17] have illustrated the analytical signal's efficacy in delineating the structural intricacies of composite materials in three dimensions, employing metrics such as instantaneous amplitude, phase, and frequency. These metrics enhance the detection of microstructural variations and defects, including ply drops, tape gaps, overlaps, wrinkles, and delaminations.

There exists, to our knowledge, an unexplored aspect concerning the influence of porosity on the analytical signal's metrics within ultrasonic testing. This identifies a research opportunity to devise methods for assessing void size and morphology distribution using monoelement ultrasonic testing. Current aerospace NDT practices primarily analyze

the signal's envelope, akin to the instantaneous amplitude. However, the prevailing systems already have the capability to operate within the analytical signal framework, predominantly employed for envelope analysis. The introduction of a porosity classification technique leveraging the analytical signal could be seamlessly integrated into existing production workflows, requiring only minor modifications to the inspection equipment, such as adjustments to the sampling frequency.

The delineation of void size and morphology distribution may also be refined by employing ultrasonic systems at diverse frequencies, acknowledging the well-established importance of wavelength in imaging. The response of voids to different frequencies, especially in estimating volume fraction, was earlier observed by Stone [40], with a focus on attenuation effects in envelope analysis. Davis et al. [101] reported on the variance in attenuation C-scans at frequencies of 1, 5, and 15 MHz in additively manufactured components, noting that defect detectability is contingent on the frequency used. For practical purposes, a frequency-based inspection methodology could be beneficial, considering the availability of transducers ranging from 1 to 15 MHz and beyond, particularly in immersion systems. Nonetheless, the practicality of executing multiple frequency inspections is constrained by time and costs considerations.

6.2 Problem definition

The size and morphology distribution of voids is a crucial factor in accurately estimating porosity levels and predicting the performance of composite materials. The problem of solely relying on attenuation for porosity evaluation is depicted in Figure 6.1. Note that the attenuation values are very similar among all coupons. On bottom, the projections of segmented porosity measured by XCT are displayed for the same 8 coupons than on top. The XCT projections show that coupons 1-4 count with different void size and morphology distribution than coupons 5-8. Ultrasonic techniques that solely rely on attenuation C-scan are incapable of providing such information.

In this chapter possible approaches for the classification of porosity based on its effect in the ultrasonic signal properties are shown. The following goals are defined:

- To identify relationships among ultrasonic properties and two distinct types of void size and morphology distribution, forming a foundation for classification.
- To address industrial inspection considerations including equipment requirements, inspection duration, and certification concerns within the discourse.

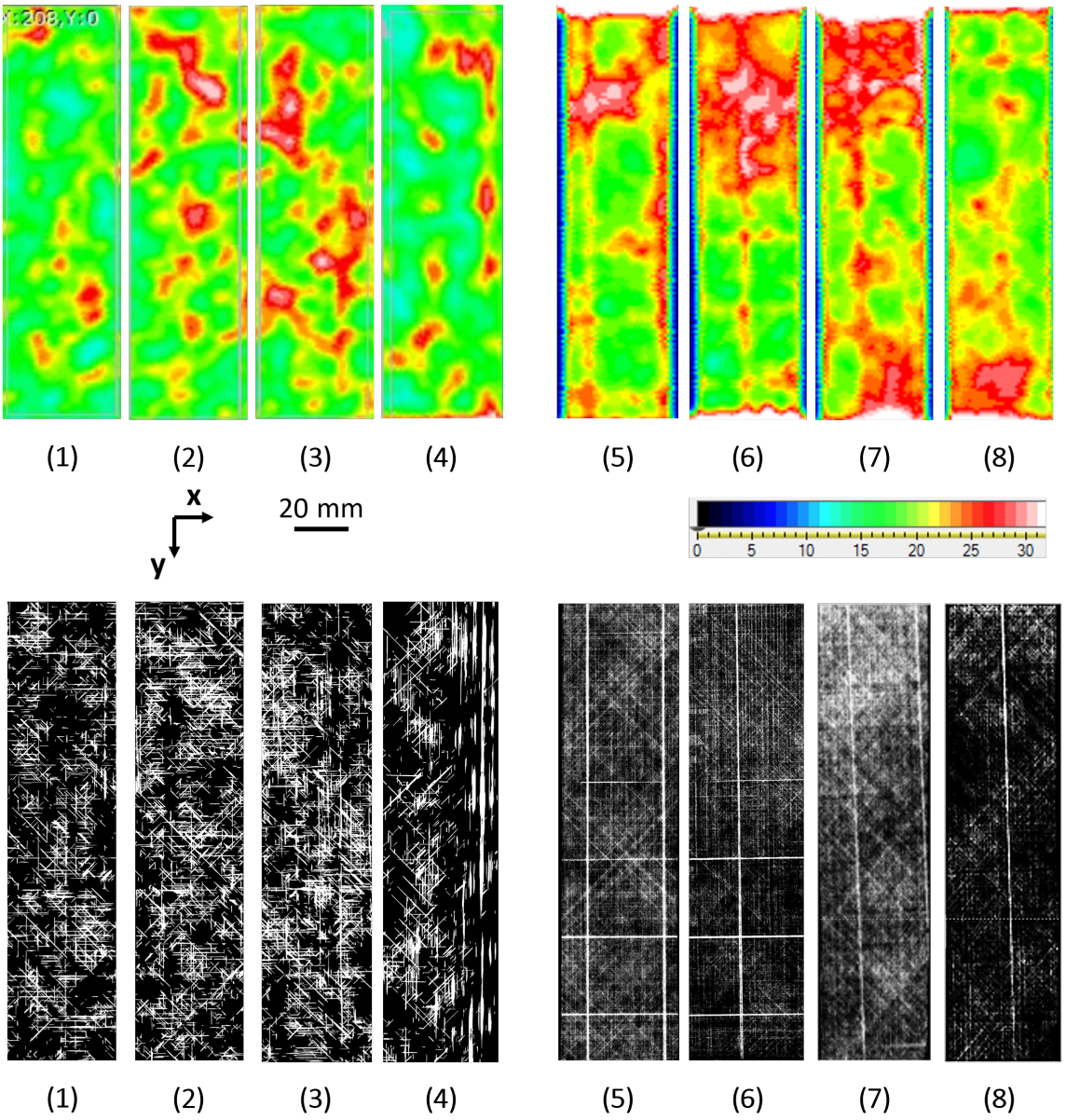

Figure 6.1: On top, the attenuation C-scan for 8 coupons of composite material are shown. Generally, the higher value of attenuation (red), the higher value of void volume fraction. Note that the attenuation values are very similar among all coupons. On bottom, the projections of segmented porosity measured by XCT are displayed for the same 8 coupons than on top. The XCT projections show that coupons 1-4 count with different void size and morphology distribution than coupons 5-8. Ultrasonic techniques that solely rely on attenuation C-scan are incapable of providing such information.

6.3 Methodology

6.3.1 Materials and characterization of porosity by XCT

TTwo different composite materials with two distinct type of porosity were used for this study. M56 composite panels were manufactured via hand-layup and cut into several coupons (1-4) as described in chapter 4. Coupon 5-8 came from a M21 resin panel manufactured by automatic fiber lay up (ATL). The curing process was performed under Double Vacuum bag Debulking (DVD), a patented method [1] to produce porosity unirformly distributed.

The coupons were tested by XCT follwing the procedure described in 4.4, which involved conducting five scans per coupon. The process of void segmentation was achieved through the implementation of local Sauvola thresholds. The procedure for coupons 1-4 is identical to the one outlined in chapter 4. For coupons 5-8 the threshold parameter that delivered the best segmentation for the Souvola local variance threshold were: radius = 10 pixels, k1 = 0.135 and k2 = 128, being k1 and k2 internal parameters of the Sauvola equations [102]

6.3.2 Ultrasonic inspections

Two advanced ultrasonic testing techniques were used for this study the effect of porosity on the analytical ultrasonic signal. The classical mono-element pulse-echo set up was not used in this study because the raw signal was not provided by the available equipment.

Air-coupled

All coupons were inspected using an air-coupled ultrasonic system, (DASEL [2]) experiments. An air-coupled transducer of central frequency equal to 0.32MHz, made also by Dasel, was used.

Phased-Array

Multiple linear arrays were employed to inspect all coupons. These arrays, as detailed in 5.3included linear arrays with frequencies of 5, 10, and 15 MHz, as well as an ultrasonic lens for the 10 MHz phase array elements. The inspections were carried out using Sitau ultrasound equipment (manufactured by Dasel, Spain) in an immersion setting for all configurations. Each array consisted of 128 elements and was oriented so that its passive direction was parallel to the major axis of the coupons. Mechanical scanning was performed in this direction using an optical encoder to measure displacement. The pulse-echo modality was utilized, employing an aperture comprising 32 elements. Except for the 5 MHz array, two parallel scans were necessary to cover the width of each coupon, which measured 40mm. These scans were manually concatenated afterward. Rescaling of the volumes was required to maintain the natural proportions of the components.

[1] https://patents.google.com/patent/US10507622B2/en
[2] https://daselsistemas.com/es/

6.3.3 Analysis of ultrasonic data

The following techniques were used for the analysis of the ultrasonic signal. Each technique was applied to both varieties of ultrasonic inspection: the linear arrays and the air-coupled method.

Traditional features: Envelope. Attenuation and amplitude C-scan

The envelop of the analytical signal is easily obtained by using equation 6.1. The equation for the analytical signal was introduced in the preliminary section and is denoted as equation 2.6. The attenuation in phased array experiments is determined by the equation denoted as 6.2. The variables A_i and A_j denote the the echo at the first material interface and the back-wall echo, respectively. In this manner, the attenuation can be defined as the measurement of the ratio between the sound that is received and the sound that departs a given material. Attenuation values may be depicted in a C-scan. The amplitude C-scan was acquired in a case of air-coupling. In comparison to immersion inspections, the use of a larger wavelength and the in-through-transmission are advantageous to the assessment of the maximum amplitude as a quality metric.

$$\Delta envelope = |x_a(t)| = |A(t)\exp(i\phi(t))| \tag{6.1}$$

$$\Delta A[db] = 2 * 10\ log\frac{A_i}{A_j} \tag{6.2}$$

Instantaneous phase and frequency

The instantaneous phase can be measured by using equation 6.3. It is the arc-tangent between the real and imaginary part of the analytical signal. The instantaneous frequency is the rate of change of the phase, it was defined in the preliminaries 2.7.

$$\phi(t) = \arctan\frac{Im(x_a)}{Re(x_a)} \tag{6.3}$$

Due to the relative novelty of these metrics their representation is not as widespread. In the references [13, 14] A or B-scan are the preferred representations, probably because it is the most useful to the determination of microstructures related with composite plies, and also, it enabled the comparison with microscopy and/or XCT cross-sectional cuts.

Fourier transform

While the utility of frequency domain analysis is well-acknowledged, its application in non-destructive testing (NDT) for composite materials remains underutilized. This limited adoption is partly due to the conventional focus on the envelope and the attenuation C-scan, which overlooks the potential insights into microstructural features like porosity that frequency domain analysis can offer. To address this gap, this study introduces a new metric, denoted as R. This metric represents an adaptation of the time-domain Sensitivity

(SNS) metric, as delineated in the work of Alvarez-Arenas et al. [103]. R is defined as follows:

$$SNS(dB) = 20\ log\frac{|FFT(V_{Rx})|}{|FFT(V_{Tx})|} \tag{6.4}$$

$$R = \frac{|FFT(V_{Mx})|}{|FFT(V_{Ax})|} \tag{6.5}$$

In the SNS case, the $|FFT(V_{Rx})|$ refers to the Fast Fourier Transform of a temporal window of the received signal. The $|FFT(V_{Tx})|$ refers to the Fast Fourier Transform of a temporal window of the emitted signal. For the calculation of R, $|FFT(V_{Mx})|$ is the FFT of the signal in a temporal window that includes only the back-wall echo (the reflection at the back of the component. $|FFT(V_{Ax})|$ is the FFT of a signal considered as the reference. It refers to the part of a signal in a temporal window that includes only the reflection at the bottom of the tank in the case where that wave has only propagated in water (not in the material). The physical interpretation is that $|FFT(V_{Ax})|$ contains the frequency distribution natural to the transducer minus the effects of the propagation in water. $|FFT(V_{Mx})|$ frequency distribution is a result of the integration of the impact of porosity and other micro-structures. For each test, the frequency distribution to be studied is restrained by the natural distribution of the transducer.

6.3.4 Proposed experiments

This section presents a structured approach for analyzing void size and morphology distribution in composite materials via ultrasonic testing methods. The primary task across these experiments involves comparing attributes of the analytic signal in regions with porosity against healthy areas for each material, corroborated by XCT data. Variations in the results are closely associated with the equipment used, which is influenced by factors such as central frequency, focal distance, beam spot size, and the setup of the testing method (e.g., pulse-echo or through-transmission).

Analysis of Instantaneous Phase and Frequency in Air-Coupled Ultrasonics

The experiment involves obtaining the instantaneous phase using air-coupled devices. To do so, all coupons were tested, the analytical signal was computed for each A-scan, subsequently the instantaneous frequency, phase and amplitude (envelope) were computed and visualize using C-scan. Then, these measurements were compared with attenuation from a 5 MHz PAUT and XCT projections of the coupons for the healthy regions and the two types of porosity types.

Analysis of Instantaneous Phase and Frequency in Phased Array Inspections

This study reproduces the previous experiment in PAUT systems. It compares the obtained C-scan of instantaneous phase and frequency obtained from linear Phased Array Ultrasonic Testing (PAUT) devices of frequencies 5 MHz, 10 MHz, 15 MHz, and 10 MHz with a lens

(as introduced in Chapter 5.1) to XCT projections in both porosity-affected and healthy regions for each material.

Frequency Domain Analysis for Porosity Detection

A Fourier transform analysis is conducted for the available PAUT systems on coupons from each material. Subsequently, the ratio R (as defined in 6.5) is calculated. In addition, for the PAUT of 5 MHz, comparisons are made between the R values at the frequency domain frequencies of 2 MHz and 5 MHz (nominal frequency), for porosity and healthy regions, again juxtaposed with XCT projections.

6.4 Results: Observed phenomena

6.4.1 Instantaneous Phase and Frequency in Air-Coupled Ultrasonics

Distinct behaviors were observed in the instantaneous phase from air-coupled ultrasonics experiments. A notable delay in the instantaneous phase was detected in areas with higher porosity concentrations, as illustrated in Figure 6.2.

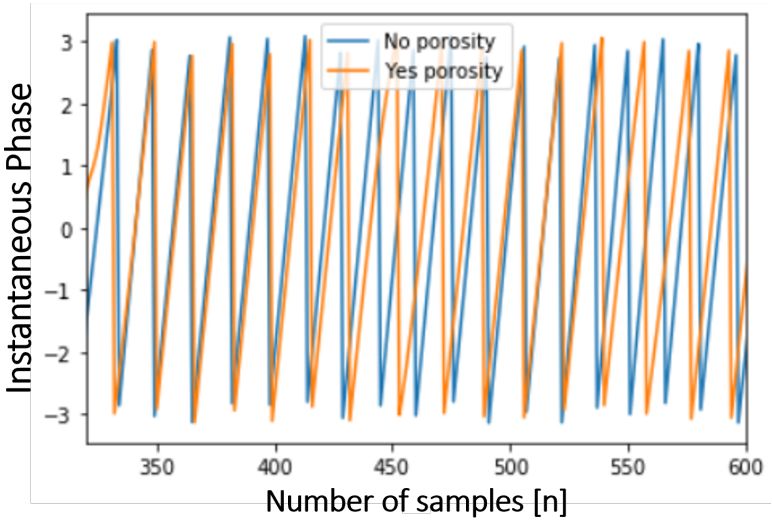

Figure 6.2: A-scan representation of the instantaneous phase for two signals measured by the air-coupled system on coupon 4. The blue signal represents an area without porosity, while the orange signal indicates an area with porosity. The starting divergence of the instantaneous phase aroung 425-450 matches to the time when ultrasonic waves starts to propagate through material thickness.

By manually selecting the sample number (x-axis in fig. 6.2 for all A-scan signal, C-scans were created from the instantaneous phase data. The delay in the porosity signals versus the healthy ones enables to obtain a clear C-scan. Darker areas in these scans correspond to regions with lower instantaneous phase values. Figure 6.3 compares XCT projections, attenuation C-scans, and instantaneous phase C-scans, highlighting differences in attenuation and instantaneous phase responses in coupons with varying porosity levels.

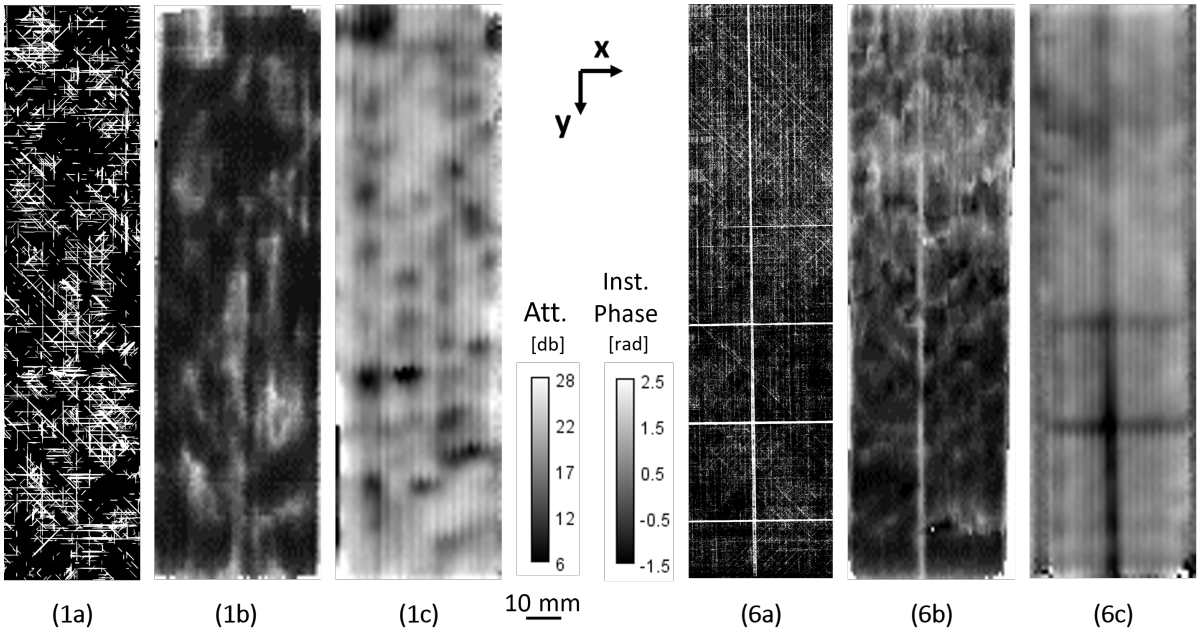

Figure 6.3: Comparative analysis of two different coupons, 1 and 6, for each material type, showcasing: a) XCT projections of porosity, b) PAUT 5 MHz attenuation, and c) the instantaneous phase for a selected sample number. In Coupon 1, regions of porosity predominantly align with areas of bright attenuation and lower instantaneous phase values. However, for Coupon 6, which features fine and dispersed porosity, high attenuation areas do not consistently correspond to lower instantaneous phase values. This discrepancy is mostly observed in regions with a lesser concentration of voids.

6.4.2 Instantaneous Frequency in Back-Wall with Phased Array

Variations in instantaneous phase and frequency were noted across different linear arrays. The central frequency and beam size were key determinants of array parameters. Porosity effects on instantaneous phase and frequency were predominantly noted in the 5 MHz linear array. A reduction in instantaneous frequency values in porosity areas compared to healthy regions was observed across all linear arrays. Yet, an approach to assess void size and morphology distribution and size was not found.

6.4.3 Frequency Domain Results for Phased Arrays

A correlation was established between the FFT of the tank bottom reflection and the central frequencies of the arrays used in inspections for both materials. Frequency distributions in porosity regions differed from healthy regions, indicating a decrease in the overall frequency spectrum. Regions in good condition showed peaks at specific frequencies, showing a high correlation with attenuation C-scans.

The frequency distribution was different among porosity regions as well. A comparative analysis was conducted on the attenuation C-scan, the C-scan of R at 2 MHz, and the C-scan of R at 5 MHz for coupons 4 and 5, based on initial experiments conducted on the relationship between instantaneous phase and frequency in air-coupled ultrasonics. Each of these entities exhibits a distinct void size and morphology distribution. (Please refer to Figure 6.5). The correspondence between the areas of significant void concentration and the attenuation and low R values (i.e., darker grey) is observed in the case of coupon 4. Nevertheless, this assertion does not hold true in the context of coupon 5. The C-scan 5c exhibits congruity just in the two elongated vertical void structures and the obliquely concentrated porosity located in the upper section of the coupon, compared to the remaining scans.

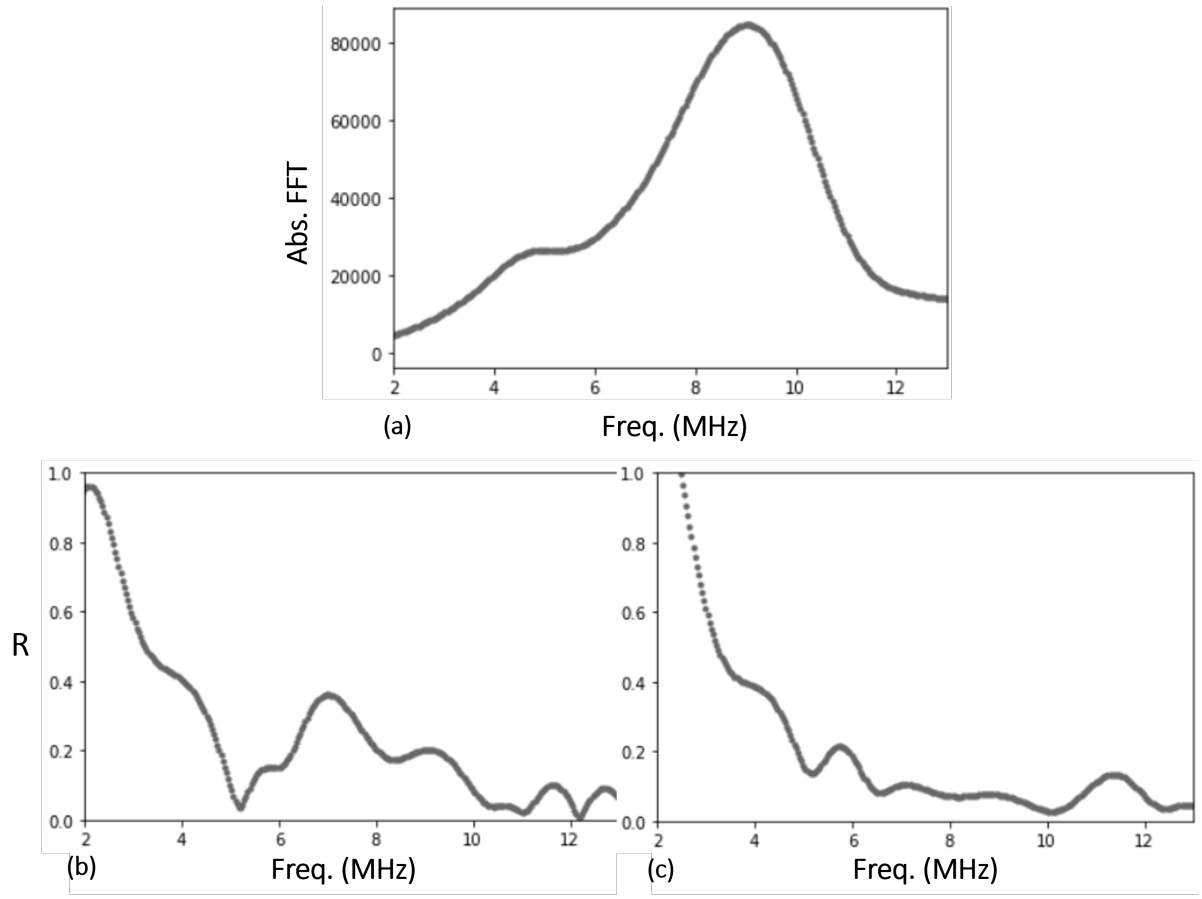

Figure 6.4: Frequency distribution analysis using the 10 MHz Phased Array Ultrasonic Testing (PAUT) system for the coupon 4, illustrating: a) The system's original frequency distribution, b) The R values for the frequency distribution of the back-wall echo in healthy regions, and c) The R values for the frequency distribution of the back-wall echo in porosity-affected regions. This comparison highlights the distinct frequency response variations between healthy and porosity-impacted areas. Similar results were obtained for M56 coupons (1-4), M21 coupones (5-8) showed very low values of R.

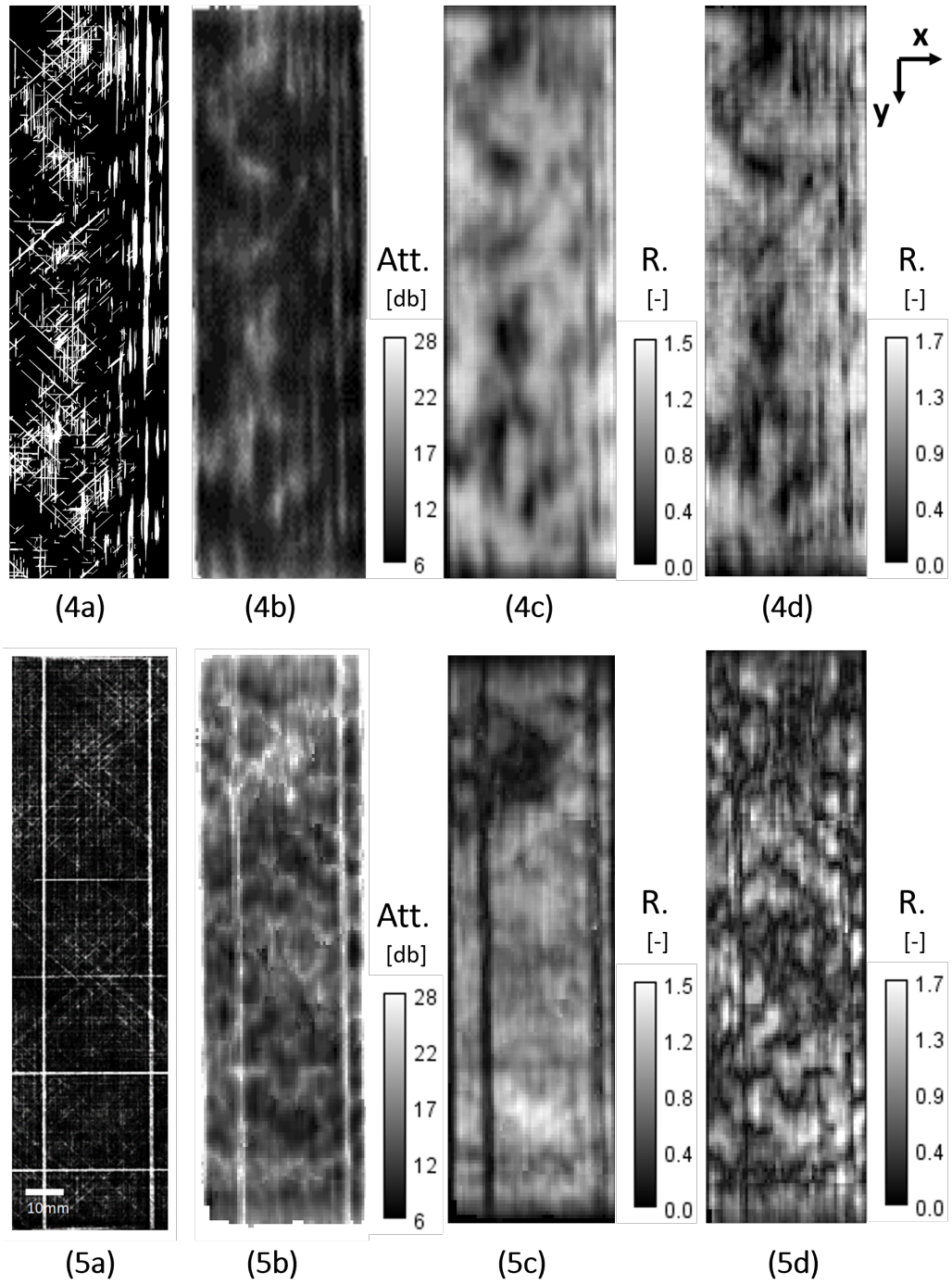

Figure 6.5: Analysis of Coupons 4 and 5, showcasing: (a) XCT imaging of segmented porosity, (b) Attenuation C-scan, (c) C-scan of R at 2 MHz, and (d) C-scan of R at 5 MHz. In Coupon 4, porosity regions are closely associated with areas showing bright attenuation and lower R values. Conversely, Coupon 5, characterized by fine and dispersed porosity, displays regions of high attenuation; however, the correlation with lower R values varies across frequencies. Specifically, in 5c, low R values are prominent only in areas with a higher concentration of voids. In contrast, 5d closely resembles the attenuation image, highlighting the frequency-dependent response of two types of observed porosity.

6.5 Discussion

The experimental findings can be summarised into three primary observations. Firstly, the air-coupled ultrasonics exhibited distinct variations in tandem instantaneous phase-attenuation for each void size and morphology distribution. Secondly, the linear arrays displayed differences in instantaneous frequency and phase. Lastly, the distribution of frequencies of the back-wall differed among the void morphologies for the linear array of 5 MHz.

The most important discovery for the classification of void size and morphology distribution through ultrasonic inspections is the distinct behaviour exhibited by the UT signal for different void characteristics for different void characteristics. This effect was found in the instantaneous phase of the 0.3 MHz air-couple system. The analysis conducted in the frequency domain involved a comparison between the R C-scan at 2 MHz and 5 MHz, as well as an assessment of the attenuation. One plausible interpretation is rooted in the impact of the correlated wavelength of the ultrasonic signals. A larger size would enable only the observation of the more sizable micro-structures, specifically the voids present in coupons 1 to 4, as well as the slender vertical air channels (typical of regions not completely filled with resin in automatic lay up -AFL- manufacturing) within coupons 5 to 8. The contrast in the effect of the void morphology is enabled by the difference in the frequency of the transducer in the first case. However, it is not enough to explain why the porosity areas produce a delay in the instantaneous phase like the one shown in the images 1c and 6c in the figure 6.5. The comparison between the impact of porosity at various frequencies was facilitated by the analysis conducted in the frequency domain in the second scenario.

Drawing from the preceding paragraph, two potential methodologies may be formulated for the classification of porosity based on its size and morphology distribution: firstly, the execution of dual inspections at varying frequencies, namely a 5 MHz transducer and a 0.3 MHz air-coupled transducer; and secondly, the execution of a singular inspection at 5 MHz, with subsequent signal processing in the frequency domain. Each of these options presents advantages and disadvantages with regard to their application in industry. In all instances, the deriving of conclusions requires the utilisation of a radiofrequency signal. Consequently, the equipment would necessitate a minimum of a software update, while others may require new electronic systems. Conducting two inspections may result in an increase in the duration of the quality process, as well as requiring the management of additional data sources and a heightened awareness of the unique aspects of inspections at varying frequencies. One advantage lies in the broad spectrum of frequencies that can be utilised, as well as the ability to employ various ultrasonic systems, including immersion and air-coupled, to investigate diverse void characteristics. Conducting inspections at a single frequency would not have any significant impact on the duration of the inspection process, nor would it require the management of multiple sources. In addition, it is anticipated that the utilisation of C-scans from either method as an input for a machine learning classifier will lead to increased automation and potentially improved outcomes. The patents related to this chapter explicate the devised methodologies for the automated computation of the aforementioned C-scans. The integration of void size and morphology distribution classification into the estimation of void volume fraction is identified as a potential area for future research. Ideally, such input would enhance the estimation of porosity quantity.

6.6 Conclusions

Numerous advancements have been made in the classification of void morphology through the use of ultrasonic inspections. Two potential methodologies were identified based on the phenomena that were observed. The initial approach involves a comparison of the attenuation C-scan obtained at a frequency of 5 MHz and the instantaneous phase C-scan acquired at a frequency of 0.32 MHz utilising an air-coupled transducer. The second method involves a comparative analysis of the C-scans pertaining to attenuation, and the R value in the frequency domain, specifically at 5 and 2 MHz.

The constraints primarily arise from a limited understanding of the fundamental mechanisms that facilitate the categorization of void size and morphology distribution. The observed phase delay in the instantaneous phase was exclusively noted in the 0.3 air-coupled transducer. A somewhat comparable pattern was detected in the 5 MHz linear array, but not in the 10 MHz. The rationale behind the necessity of conducting the analysis of R within a 2 MHz range remains unclear. There may be a correlation between the classification of void morphology and the necessary associated wavelength of ultrasonic inspections. This is a relevant future line of work for the generalization of the methodology. In situations where there are varying sizes of voids, an additional set of frequencies may be necessary. Incorporating the established capabilities of these techniques into a machine learning classification model is likely to enhance automation and yield superior outcomes. The integration of these techniques in estimating porosity levels may necessitate the adaptation of models to void morphology.

Chapter 7

Conclusions and Future Work

7.1 Conclusions

The porosity is one of the most important defects in the manufacturing of composite materials. Among the various NDT methods, Ultrasonic Testing (UT) is favored for its cost-effectiveness and ease of implementation during in-service inspections. Despite substantial investments in ensuring quality standards and developing porosity-free production processes, UT methods for porosity evaluation have been limited in scope and precision. The use of X-ray computed tomography and data science methods show great future in overcoming current ultrasonic limitations. The thesis tackled two areas of porosity assessment: the improvement of the void volume estimation, and the assessment of void size and morphology.

7.1.1 Improvement of the estimation of void volume using data science methods.

A data-driven methodology to estimate void volume fraction using ultrasounds and X-ray computed tomography was presented:

- The estimation of void volume fraction was framed as a supervised regression task where ultrasonic features are used to predict the void volume measured by XCT. Experiments were performed for four coupons of carbon fibre reinforced polymer with varying levels of porosity.
- Our proposed methodology marks a methodological advancement in analyzing the relationship between ultrasonic data and XCT void volume fraction. The approach enables the obtention of an extensive dataset, which enables deeper analysis of porosity distribution compared to existing methods.
- Four machine learning models were trained using cross-validation linear regression, multilinear regression, regression tree, and random forest. Special attention was paid to the model's explainability and error evaluation. For the error assessment, data visualisation approaches were suggested.

7.1.2 Goals and research questions related to estimation of void volume

Based on the results and concerning the research questions withing Objective 1: Refine Porosity Estimation in Ultrasonic Testing through Data Science Integration:

- Research Question 1.1: How effectively can machine learning algorithms, utilizing attenuation C-scan images, predict the void volume fraction in composite materials?

  A linear model effectively explains the void volume fraction using attenuation for a specific coupon. This relation is affected by the size of the filter where XCT void volume is measured, and it is probably link to the ultrasonic beam spot size. However, the suitability of using the lineal model attenuation-void vol. to predict in unseen data is limited; it lacks generalization capability. In this context, attenuation serves as a descriptive tool for void volume fraction in a single coupon. However, the linear model exhibits underfitting, failing to capture the variability in the relationship between attenuation and void volume fraction across diverse coupons. The use of several ultrasonic features proves to yield better estimates. In this regard, the multilineal models show better estimations of the regions with higher values of void vol., while the random forest predicts better in regions with low or no-porosity.

- Research Question 1.2: Which ultrasonic features are most critical in the machine learning-based estimation of void volume fraction for enhanced porosity assessment?

  The feature selection process showed that attributes linked to the amplitude and attenuation of the backwall echo were the most relevant. This results were expected since they have phisical interpretation. Other important features are related to the echo from the bottom of the tank.

7.1.3 Assessment of void size and morphology.

The data driven methodology presented a highly precise methodology for analyzing porosity. However, it does not fully consider void morphology's impact on void volume fraction estimatio. None of the attributes used offer insights into this aspect, which is crucial for accurate void volume estimation. To solve this challenge two lines of work were developed:

Imaging and segmentation of voids.

The first line of work consisted in developing a methodology to segment voids in 3D ultrasonic data using convolutional neural networks (CNN) and XCT was developed:

- So far, research in porosity evaluation has been limited to estimating the void volume portion. However, the distribution of the porosity along the thickness is a demanded feature from the industry. Several ultrasonic systems were developed in this thesis, including a monoelement 5 MHz transducer, linear arrays of 5, 10, and 15 MHz, and a 0.3 MHz air-coupled transducer, and their findings were compared to the XCT volumes.

- The ultrasonic examination was optimized by using a 10 MHz linear array with a lens to focus in the passive direction. Voids down to a few hundred micrometers

were clearly apparent, allowing coincidences between voids identified in the XCT and this linear array pictures to be established.

- A mechanism for 3D void segmentation was proposed. It entailed registering the XCT and UT pictures in order to build a convolutional neural network that performs void classification. Despite the fact that the results demonstrate the possibility of such a method for the available dataset, further work is needed to deal with false positives, increase the signal-to-noise ratio, and alleviate signal attenuation as it propagates through the thickness of the material.

Classification of porosity using ultrasonic attributes.

The second line of work consisted in performing investigations of the impact of two types of porosity morphology in the analytical signal attributes, to do so, several ultrasonic tests were carried out:

- Coupons of different type of carbon fibre reinforced polymer were tested by air-coupled, monoelement, phased array ultrasonic systems and XCT. Each composite showed a distinct type of porosity, the M56 showed large elipsoidal voids, while the M21, finer and dispersed voids, also some very large, thin and plain voids.
- Analytical signal analysis were performed for the results of each testing equipment, obtaining the instantaneous phase, frequency and amplitude. Also, analysis in the frequency domain were performed.
- Results show that the instantaneous phase is delayed in regions with porosity with respect to healthy regions, furthermore, that only occurs for certain porosity regions, showing in all the cases for the coupons of M56, but not in all the variety of porosity regions for M21 coupons.
- Fourier analysis also displayed differences between the porosity and healthy regions, and differences due the porosity of M56 and M21 coupons were obtained if the frequency domain is study near the 2 MHz region. Results that resemblant to the instantaneous phase in air-coupled devices, yet they are different.

7.1.4 Goals and research questions related to the assessment of void size and morphology.

For Objective 2: Establish Innovative Methodologies for Comprehensive Porosity Characterization in Composite Materials:

- Research Question 2.1: What novel approaches can data science, particularly machine learning, offer in the qualitative characterization of porosity morphology in composites?

  It has been proved that porosity down to few hundred of micrometers is visible using lineal PAUT systems, although this is highly dependant on factors like the distance of the void to the front face of the coupon, the nearby voids, orientation in the plane. Optimization of the testing procedures is key to visualize specially challenging cases like thin voids in ± 45 or regions with high density of voids. In

this sense, the gain of methods to focus in the passive direction such as the used lens, are vital. Other possible approaches could consist in the use of matrix PAUT systems. This results alone are a solution to assess the porosity, yet the analysis of 3D volumes would require of time and expert stuff. The segmentation of voids, as a necessary step to calculate quantitative metrics of the voids is desirable. In this sense the proposed methodology and the CNN's show promising results, althought they need to be improved.

Certainly, for monoelement UT the 3D visualization and segmentation of voids is most probably not possible for most of the porosity cases. Yet another options to characterize void morphology would consist in the explotaitation of the proposed analytical signal and Fourier analysis. In this regard, the use of inst. phase in air-coupled devices would enable to perform certain qualitative assessment of porosity, while enjoying the advantages of the technique. For immersion systems, the proposed comparison of the response for different frequencies, would enable certain assessment of porosity size and distribution.

7.2 Future work

While this thesis has achieved its set objectives, it has also paved the way for several new research avenues, as outlined below:

1. **Ultrasonic testing-XCT Registration:**
   - This is a pivotal task across various research lines. Developing automated 3D registration methods is essential for generating better and more extensive datasets.
2. **Data-Driven Methodology:**
   - Expansion of the dataset for void estimation is necessary in multiple dimensions. Investigating additional composite materials and assessing the impact of material thickness are critical. Concurrently, exploring the application of neural networks and explainable machine learning techniques is a promising research direction.
3. **Integration of Void Morphology-Aware Features:**
   - Automating porosity classification based on morphology features using machine learning models is a potential area of exploration. The described methodologies provide a framework for obtaining C-scans of void-morphology-aware features, which could be seamlessly integrated into the data-driven methodology. This integration would allow for more nuanced void volume estimations tailored to different porosity types.
4. **3D Imaging and Segmentation of Voids Using UT:**
   - Key research areas include addressing attenuation in propagation through material thickness and optimizing inspection parameters, such as employing matrix phased arrays. Enhancing imaging quality will benefit void segmentation, but expanding the dataset is necessary for training more sophisticated convolutional networks. Additionally, object detection to assess the impact of void morphology

on detection is an intriguing research topic.

5. **Analytical-Signal and Void Morphology:**
    - The observed delay in the instantaneous phase using a 0.3 MHz air-coupled transducer in porosity areas warrants further investigation to understand the underlying mechanisms and to identify the frequency and coupon thickness ranges where this phenomenon is observable. While variations in instantaneous phase and frequency depending on inspection frequency for resin-rich layer detection are known, assessing these effects in the presence of porosity requires additional research.

Automatic defect detection was beyond the scope of this thesis. However, the current trend in applying machine learning to non-destructive testing (NDT) is increasingly leaning towards deep learning for automating defect detection. A significant future research direction could involve developing such methods for common defects in composite materials, including porosity, delaminations, and others. This direction is likely to align with the future needs of NDT companies. This thesis lays a solid foundation for all this future research in data-driven methods for NDT. By exploring these potential research areas, we can meet the demands of various stakeholders, contributing to more efficient manufacturing, safer transport, and more robust structures.

Bibliography

[1] E A Birt and R A Smith. "A Review of NDE Methods for Porosity". In: *Insight - Non-Destructive Testing and Condition Monitoring* 46.11 (Nov. 2004), pp. 681–686. DOI: 10.1784/insi.46.11.681.52280.

[2] R A Smith. "Composite Defects and Their Detection". In: *MATERIALS SCIENCE AND ENGINEERING* (), p. 14.

[3] FSTJ Editorial Office. "Imagification Technology and Deep Learning Accelerating Defect Detection in Non-Destructive Testing for Wind Turbine Blades". In: *FUJITSU Sci. Tech. J.* 55.2 (2019), p. 7.

[4] Ahmad Osman. "Automated Evaluation of Three Dimensional Ultrasonic Datasets". In: (2013), p. 187.

[5] Maryam Shafiei Alavijeh et al. "NDE 4.0 Compatible Ultrasound Inspection of Butt-Fused Joints of Medium-Density Polyethylene Gas Pipes, Using Chord-Type Transducers Supported by Customized Deep Learning Models". In: *Research in Nondestructive Evaluation* 31.5-6 (Nov. 2020), pp. 290–305. DOI: 10.1080/09349847.2020.1841864.

[6] Iikka Virkkunen et al. "Augmented Ultrasonic Data for Machine Learning". In: *Journal of Nondestructive Evaluation* 40.1 (Mar. 2021), p. 4. DOI: 10.1007/s10921-020-00739-5.

[7] Richard J. Pyle et al. "Deep Learning for Ultrasonic Crack Characterization in NDE". In: *IEEE Transactions on Ultrasonics, Ferroelectrics, and Frequency Control* 68.5 (May 2021), pp. 1854–1865. DOI: 10.1109/TUFFC.2020.3045847.

[8] Daniel Sparkman et al. "A Supervised Learning Approach for Prediction of X-Ray Computed Tomography Data from Ultrasonic Testing Data". In: *45TH Annual Review Of Progress In Quantitative Nondestructive Evaluation, Volume 38*. Vermont, USA, 2019, p. 030002. DOI: 10.1063/1.5099748.

[9] Yuechao Chen et al. "CFRP Voids 3D Identification and Location Method Based on the Process of Backscattered Signal". In: *Journal of Wuhan University of Technology-Mater. Sci. Ed.* 31.1 (Feb. 2016), pp. 172–177. DOI: 10.1007/s11595-016-1348-1.

[10] D. Gabor. "Theory of Communication. Part 1: The Analysis of Information". In: *Journal of the Institution of Electrical Engineers - Part III: Radio and Communication Engineering* 93.26 (Nov. 1946), pp. 429–441. DOI: 10.1049/ji-3-2.1946.0074.

[11] Paul M Gammell. "The Analytic Signal Magnitude for Improved Ultrasonic Signatures". In: ().

[12] R. C. Heyser. "Time Delay Spectrometry". In: *The Journal of the Acoustical Society of America* 53.1 (Jan. 1973), pp. 319–320. DOI: 10.1121/1.1982305.

[13] Robert A. Smith et al. "Ultrasonic Tracking of Ply Drops in Composite Laminates". In: *42ND Annual Review Of Progress In Quantitative Nondestructive Evaluation:*

Incorporating the 6th European-American Workshop on Reliability of NDE. Minneapolis, Minnesota, 2016, p. 050006. DOI: 10.1063/1.4940505.

[14] Robert A. Smith et al. "Ultrasonic Analytic-Signal Responses From Polymer-Matrix Composite Laminates". In: *IEEE Transactions on Ultrasonics, Ferroelectrics, and Frequency Control* 65.2 (Feb. 2018), pp. 231–243. DOI: 10.1109/TUFFC.2017.2774776.

[15] L.J. Nelson, R.A. Smith, and M. Mienczakowski. "Ply-Orientation Measurements in Composites Using Structure-Tensor Analysis of Volumetric Ultrasonic Data". In: *Composites Part A: Applied Science and Manufacturing* 104 (Jan. 2018), pp. 108–119. DOI: 10.1016/j.compositesa.2017.10.027.

[16] Beatriz Larrañaga-Valsero et al. "Wrinkle Measurement in Glass-Carbon Hybrid Laminates Comparing Ultrasonic Techniques: A Case Study". In: *Composites Part A: Applied Science and Manufacturing* 114 (Nov. 2018), pp. 225–240. DOI: 10.1016/j.compositesa.2018.08.014.

[17] Xiaoyu Yang et al. "Parametric Study on Interply Tracking in Multilayer Composites by Analytic-Signal Technology". In: *Ultrasonics* 111 (Mar. 2021), p. 106315. DOI: 10.1016/j.ultras.2020.106315.

[18] F. Sket et al. "Determination of Damage Micromechanisms and Fracture Resistance of Glass Fiber/Epoxy Cross-Ply Laminate by Means of X-ray Computed Microtomography". In: *Composites Science and Technology* 72.2 (Jan. 2012), pp. 350–359. DOI: 10.1016/j.compscitech.2011.11.025.

[19] A-F. Obaton et al. "In Vivo XCT Bone Characterization of Lattice Structured Implants Fabricated by Additive Manufacturing". In: *Heliyon* 3.8 (Aug. 2017), e00374. DOI: 10.1016/j.heliyon.2017.e00374.

[20] Alex Krizhevsky, Ilya Sutskever, and Geoffrey E. Hinton. "ImageNet Classification with Deep Convolutional Neural Networks". In: *Communications of the ACM* 60.6 (May 2017), pp. 84–90. DOI: 10.1145/3065386.

[21] Ashish Vaswani et al. *Attention Is All You Need*. Dec. 2017. arXiv: 1706.03762 [cs].

[22] Aditya Ramesh et al. *Hierarchical Text-Conditional Image Generation with CLIP Latents*. Apr. 2022. arXiv: 2204.06125 [cs].

[23] David Forsyth and Jean Ponce. *Computer Vision: A Modern Approach*. 2nd ed. Boston: Pearson, 2012.

[24] Abhishek Balasubramaniam and Sudeep Pasricha. "Object Detection in Autonomous Vehicles: Status and Open Challenges". In: (), p. 6.

[25] P. Viola and M. Jones. "Rapid Object Detection Using a Boosted Cascade of Simple Features". In: *Proceedings of the 2001 IEEE Computer Society Conference on Computer Vision and Pattern Recognition. CVPR 2001*. Vol. 1. Kauai, HI, USA: IEEE Comput. Soc, 2001, pp. I-511-I–518. DOI: 10.1109/CVPR.2001.990517.

[26] Karen Simonyan and Andrew Zisserman. *Very Deep Convolutional Networks for Large-Scale Image Recognition*. Apr. 2015. arXiv: 1409.1556 [cs].

[27] Kaiming He et al. *Deep Residual Learning for Image Recognition*. Dec. 2015. arXiv: 1512.03385 [cs].

[28] Christian Szegedy et al. *Going Deeper with Convolutions*. Sept. 2014. arXiv: 1409.4842 [cs].

[29] Joseph Redmon et al. *You Only Look Once: Unified, Real-Time Object Detection*. May 2016. arXiv: 1506.02640 [cs].

[30] Ross Girshick et al. *Rich Feature Hierarchies for Accurate Object Detection and Semantic Segmentation*. Oct. 2014. arXiv: 1311.2524 [cs].

[31] Ross Girshick. *Fast R-CNN*. Sept. 2015. arXiv: 1504.08083 [cs].

[32] Shaoqing Ren et al. *Faster R-CNN: Towards Real-Time Object Detection with Region Proposal Networks*. Jan. 2016. arXiv: 1506.01497 [cs].

[33] Kaiming He et al. *Mask R-CNN*. Jan. 2018. arXiv: 1703.06870 [cs].

[34] Mahoor Mehdikhani et al. "Voids in Fiber-Reinforced Polymer Composites: A Review on Their Formation, Characteristics, and Effects on Mechanical Performance". In: *Journal of Composite Materials* 53 (2018). DOI: 10.1177/0021998318772152.

[35] H. Jeong. "Effects of Voids on the Mechanical Strength and Ultrasonic Attenuation of Laminated Composites". In: *Journal of Composite Materials* 31.3 (Feb. 1997), pp. 276–292. DOI: 10.1177/002199839703100303.

[36] Michelle Leali Costaa, Sergio Frascino M. de Almeidaa, and Mirabel Cerqueira Rezendeb. "The Influence of Porosity on the Interlaminar Shear Strength of Carbon/Epoxy and Carbon/Bismaleimide Fabric Laminates". In: *Composites Science and Technology* 61 (2001).

[37] Yutong Fu and Xuefeng Yao. "A Review on Manufacturing Defects and Their Detection of Fiber Reinforced Resin Matrix Composites". In: *Composites Part C: Open Access* 8 (Aug. 2022), p. 100276. DOI: 10.1016/j.jcomc.2022.100276.

[38] Christian Garnier et al. "The Detection of Aeronautical Defects in Situ on Composite Structures Using Non Destructive Testing". In: *Composite Structures* 93.5 (Apr. 2011), pp. 1328–1336. DOI: 10.1016/j.compstruct.2010.10.017.

[39] Janez Rus et al. "Qualitative Comparison of Non-Destructive Methods for Inspection of Carbon Fiber-Reinforced Polymer Laminates". In: *Journal of Composite Materials* 54.27 (Nov. 2020), pp. 4325–4337. DOI: 10.1177/0021998320931162.

[40] D.E.W. Stone and B. Clarke. "Ultrasonic Attenuation as a Measure of Void Content in Carbon-Fibre Reinforced Plastics". In: *Non-Destructive Testing* 8.3 (June 1975), pp. 137–145. DOI: 10.1016/0029-1021(75)90023-7.

[41] D. K. Hsu and S. M. Nair. "Evaluation of Porosity in Graphite-Epoxy Composite by Frequency Dependence of Ultrasonic Attenuation". In: *Review of Progress in Quantitative Nondestructive Evaluation*. Ed. by Donald O. Thompson and Dale E. Chimenti. Boston, MA: Springer US, 1987, pp. 1185–1193. DOI: 10.1007/978-1-4613-1893-4_135.

[42] B.G. Martin. "Ultrasonic Attenuation Due to Voids in Fibre-Reinforced Plastics". In: *NDT International* 9.5 (Oct. 1976), pp. 242–246. DOI: 10.1016/0308-9126(76)90004-3.

[43] Shanshan Ding et al. "Investigations on Relationship between Porosity and Ultrasonic Attenuation Coefficient in CFRP Laminates Based on RMVM". In: (2015), p. 9.

[44] Li Lin, Ming Luo, and Hongtao Tian. "Experimental Investigation on Porosity of Carbon Fiber-Reinforced Composite Using Ultrasonic Attenuation Coefficient". In: (2008), p. 9.

[45] S. Hernández et al. "Effect of Curing Cycle on Void Distribution and Interlaminar Shear Strength in Polymer-Matrix Composites". In: *Composites Science and Technology* 71.10 (July 2011), pp. 1331–1341. DOI: 10.1016/j.compscitech.2011.05.002.

[46] A. Isaac et al. "In Situ 3D Quantification of the Evolution of Creep Cavity Size, Shape, and Spatial Orientation Using Synchrotron X-ray Tomography". In: *Materi-*

als Science and Engineering: A 478.1-2 (Apr. 2008), pp. 108–118. DOI: 10.1016/j.msea.2007.05.108.

[47] J Kastner et al. "Defect and Porosity Determination of Fibre Reinforced Polymers by X-ray Computed Tomography". In: (), p. 12.

[48] Federico Sket et al. "Effect of Hydrostatic Pressure on the 3D Porosity Distribution and Mechanical Behavior of a High Pressure Die Cast Mg AZ91 Alloy". In: *Metallurgical and Materials Transactions A* 46.9 (Sept. 2015), pp. 4056–4069. DOI: 10.1007/s11661-015-3024-z.

[49] Josef Krautkrämer and Herbert Krautkrämer. *Ultrasonic Testing of Materials*. Berlin, Heidelberg: Springer Berlin Heidelberg, 1990. DOI: 10.1007/978-3-662-10680-8.

[50] J Welter, J Aldrin, and D Forsyth. "Automated Data Analysis (ADA) of Ultrasonic NDE Data for Composites". In: (), p. 10.

[51] Michał Stefaniuk and Krzysztof Dragan. "Improvements to Image Processing Algorithms Used for Delamination Damage Extraction and Modeling". In: (2016). DOI: 10.13140/RG.2.1.5096.6001.

[52] Tj Barry et al. "Defect Characterisation in Laminar Composite Structures Using Ultrasonic Techniques and Artificial Neural Networks". In: *Journal of Composite Materials* 50.7 (Mar. 2016), pp. 861–871. DOI: 10.1177/0021998315584651.

[53] Jiaxing Ye, Shunya Ito, and Nobuyuki Toyama. "Computerized Ultrasonic Imaging Inspection: From Shallow to Deep Learning". In: *Sensors* 18.11 (Nov. 2018), p. 3820. DOI: 10.3390/s18113820.

[54] John C. Aldrin and David S. Forsyth. "Demonstration of Using Signal Feature Extraction and Deep Learning Neural Networks with Ultrasonic Data for Detecting Challenging Discontinuities in Composite Panels". In: *45TH Annual Review Of Progress In Quantitative Nondestructive Evaluation, Volume 38*. Vermont, USA, 2019, p. 020012. DOI: 10.1063/1.5099716.

[55] Luka Posilovic et al. "Flaw Detection from Ultrasonic Images Using YOLO and SSD". In: *2019 11th International Symposium on Image and Signal Processing and Analysis (ISPA)* (2019). DOI: 10.1109/ispa.2019.8868929.

[56] John C. Aldrin et al. "Pitch-Catch Ultrasonic Array Characterization of the Hidden Region of Impact Damage in Composites". In: *Research in Nondestructive Evaluation* 31.5-6 (Nov. 2020), pp. 275–289. DOI: 10.1080/09349847.2020.1847374.

[57] Alexander C. S. Douglass, Daniel Sparkman, and Joel B. Harley. "Segmentation of Hidden Delaminations with Pitch–Catch Ultrasonic Testing and Agglomerative Clustering". In: *Journal of Nondestructive Evaluation* 39.1 (Mar. 2020), p. 8. DOI: 10.1007/s10921-019-0649-7.

[58] Huifang Xiao et al. "Defects Identification Using the Improved Ultrasonic Measurement Model and Support Vector Machines". In: *NDT & E International* 111 (Apr. 2020), p. 102223. DOI: 10.1016/j.ndteint.2020.102223.

[59] Jiaxing Ye and Nobuyuki Toyama. "Benchmarking Deep Learning Models for Automatic Ultrasonic Imaging Inspection". In: *IEEE Access* 9 (2021), pp. 36986–36994. DOI: 10.1109/ACCESS.2021.3062860.

[60] Thibault Latête, Baptiste Gauthier, and Pierre Belanger. "Towards Using Convolutional Neural Network to Locate, Identify and Size Defects in Phased Array Ultrasonic Testing". In: *Ultrasonics* 115 (Aug. 2021), p. 106436. DOI: 10.1016/j.ultras.2021.106436.

[61] Nathaniel J. Blackman, David A. Jack, and Benjamin M. Blandford. "Improvement in the Quantification of Foreign Object Defects in Carbon Fiber Laminates Using Immersion Pulse-Echo Ultrasound". In: *Materials* 14.11 (May 2021), p. 2919. DOI: 10.3390/ma14112919.

[62] Walter Nsengiyumva et al. "Advances, Limitations and Prospects of Nondestructive Testing and Evaluation of Thick Composites and Sandwich Structures: A State-of-the-Art Review". In: *Composite Structures* 256 (Jan. 2021), p. 112951. DOI: 10.1016/j.compstruct.2020.112951.

[63] Etienne Provencal and Luc Laperrière. "WeldNet: From 3D Phased-Array Ultrasound Scans to 3D Geometrical Models of Welds and Defects". In: *CIRP Annals* 71.1 (2022), pp. 445–448. DOI: 10.1016/j.cirp.2022.04.033.

[64] Luka Posilović et al. "Generative Adversarial Network with Object Detector Discriminator for Enhanced Defect Detection on Ultrasonic B-scans". In: *Neurocomputing* 459 (Oct. 2021), pp. 361–369. DOI: 10.1016/j.neucom.2021.06.094. arXiv: 2106.04281 [cs, eess].

[65] Sergio Cantero-Chinchilla, Paul D. Wilcox, and Anthony J. Croxford. "Deep Learning in Automated Ultrasonic NDE – Developments, Axioms and Opportunities". In: *NDT & E International* 131 (Oct. 2022), p. 102703. DOI: 10.1016/j.ndteint.2022.102703. arXiv: 2112.06650 [eess].

[66] Nauman Munir et al. "Performance Enhancement of Convolutional Neural Network for Ultrasonic Flaw Classification by Adopting Autoencoder". In: *NDT & E International* 111 (Apr. 2020), p. 102218. DOI: 10.1016/j.ndteint.2020.102218.

[67] Fei Gao et al. "Ultrasonic Signal Denoising Based on Autoencoder". In: *Review of Scientific Instruments* 91.4 (Apr. 2020), p. 045104. DOI: 10.1063/1.5136269.

[68] Jianxiao Mao, Hao Wang, and Billie F Spencer. "Toward Data Anomaly Detection for Automated Structural Health Monitoring: Exploiting Generative Adversarial Nets and Autoencoders". In: *Structural Health Monitoring* 20.4 (July 2021), pp. 1609–1626. DOI: 10.1177/1475921720924601.

[69] Georgios Pilikos et al. "Deep Data Compression for Approximate Ultrasonic Image Formation". In: *2020 IEEE International Ultrasonics Symposium (IUS)*. Sept. 2020, pp. 1–4. DOI: 10.1109/IUS46767.2020.9251753. arXiv: 2009.02293 [cs, eess].

[70] Manasa Kesharaju and Romesh Nagarajah. "Feature Selection for Neural Network Based Defect Classification of Ceramic Components Using High Frequency Ultrasound". In: *Ultrasonics* 62 (Sept. 2015), pp. 271–277. DOI: 10.1016/j.ultras.2015.05.027.

[71] Georgios Pilikos et al. "Fast Ultrasonic Imaging Using End-to-End Deep Learning". In: *2020 IEEE International Ultrasonics Symposium (IUS)*. Las Vegas, NV, USA: IEEE, Sept. 2020, pp. 1–4. DOI: 10.1109/IUS46767.2020.9251550.

[72] K. Supreet Alguri and Joel B. Harley. "Transfer Learning of Ultrasonic Guided Waves Using Autoencoders: A Preliminary Study". In: *45TH Annual Review Of Progress In Quantitative Nondestructive Evaluation, VOLUME 38*. Vermont, USA, 2019, p. 050013. DOI: 10.1063/1.5099779.

[73] Yongmin Guo et al. "Fully Convolutional Neural Network With GRU for 3D Braided Composite Material Flaw Detection". In: *IEEE Access* 7 (2019), pp. 151180–151188. DOI: 10.1109/ACCESS.2019.2946447.

[74] Meng Yuan et al. "Automatic Recognition and Positioning of Wheel Defects in Ultrasonic B-scan Image Using Artificial Neural Network and Image Processing".

In: *Journal of Testing and Evaluation* 48 (Jan. 2020), p. 20180545. DOI: 10.1520/JTE20180545.

[75] Fairouz Bettayeb, Tarek Rachedi, and Hamid Benbartaoui. "An Improved Automated Ultrasonic NDE System by Wavelet and Neuron Networks". In: *Ultrasonics* 42.1-9 (Apr. 2004), pp. 853–858. DOI: 10.1016/j.ultras.2004.01.064.

[76] Roberto Miorelli et al. "Defect Sizing in Guided Wave Imaging Structural Health Monitoring Using Convolutional Neural Networks". In: *NDT & E International* 122 (Sept. 2021), p. 102480. DOI: 10.1016/j.ndteint.2021.102480.

[77] Homin Song and Yongchao Yang. "Super-Resolution Visualization of Subwavelength Defects via Deep Learning-Enhanced Ultrasonic Beamforming: A Proof-of-Principle Study". In: *NDT & E International* 116 (2020). DOI: 10.1016/j.ndteint.2020.102344.

[78] Joaquín Fernández-León et al. "A Machine Learning Strategy for Race-Tracking Detection During Manufacturing of Composites by Liquid Moulding". In: *Integrating Materials and Manufacturing Innovation* 11.2 (June 2022), pp. 296–311. DOI: 10.1007/s40192-022-00263-6.

[79] John C Aldrin. "Intelligence Augmentation and Human Machine Interface (HMI) Best Practices for NDT 4.0 Reliability". In: (2019). DOI: 10.13140/RG.2.2.28149.93929.

[80] John C. Aldrin and Eric A. Lindgren. "The Need and Approach for Characterization - U.S. Air Force Perspectives on Materials State Awareness". In: *44TH Annual Review Of Progress In Quantitative Nondestructive Evaluation, Volume 37*. Provo, Utah, USA, 2018, p. 020004. DOI: 10.1063/1.5031501.

[81] Norbert G Meyendorf. "NDE 4.0—NDE for the 21st Century—The Internet of Things and Cyber Physical Systems Will Revolutionize NDE". In: (), p. 10.

[82] N. Brierley et al. "Advances in the UK Toward NDE 4.0". In: *Research in Nondestructive Evaluation* 31.5-6 (Nov. 2020), pp. 306–324. DOI: 10.1080/09349847.2020.1834657.

[83] Johannes Vrana. "NDE 4.0: The Fourth Revolution in Non-Destructive Evaluation: Digital Twin, Semantics, Interfaces, Networking, Feedback, New Markets and Integration into the Industrial Internet of Things". In: (2019). DOI: 10.13140/RG.2.2.17635.50720.

[84] R. Parasuraman, T.B. Sheridan, and C.D. Wickens. "A Model for Types and Levels of Human Interaction with Automation". In: *IEEE Transactions on Systems, Man, and Cybernetics - Part A: Systems and Humans* 30.3 (May 2000), pp. 286–297. DOI: 10.1109/3468.844354.

[85] Renato M. Assunção and Edna A. Reis. "A New Proposal to Adjust Moran'sI for Population Density". In: *Statistics in Medicine* 18.16 (Aug. 1999), pp. 2147–2162. DOI: 10.1002/(SICI)1097-0258(19990830)18:16<2147::AID-SIM179>3.0.CO;2-I.

[86] Roger S. Bivand and David W. S. Wong. "Comparing Implementations of Global and Local Indicators of Spatial Association". In: *TEST* 27.3 (Sept. 2018), pp. 716–748. DOI: 10.1007/s11749-018-0599-x.

[87] L F Kozachenko and N N Leonenko. "Sample Estimate of the Entropy of a~Random Vector". In: (1987), p. 9.

[88] Alexander Kraskov, Harald Stoegbauer, and Peter Grassberger. "Estimating Mutual Information". In: *Physical Review E* 69.6 (June 2004), p. 066138. DOI: 10.1103/PhysRevE.69.066138. arXiv: cond-mat/0305641.

[89] Brian C. Ross. "Mutual Information between Discrete and Continuous Data Sets". In: *PLoS ONE* 9.2 (Feb. 2014). Ed. by Daniele Marinazzo, e87357. DOI: 10.1371/journal.pone.0087357.

[90] Isabelle Guyon, Jason Weston, and Stephen Barnhill. "Gene Selection for Cancer Classification Using Support Vector Machines". In: (2002), p. 34.

[91] Ignacio Arganda-Carreras et al. "Consistent and Elastic Registration of Histological Sections Using Vector-Spline Regularization". In: *Computer Vision Approaches to Medical Image Analysis*. Ed. by David Hutchison et al. Vol. 4241. Berlin, Heidelberg: Springer Berlin Heidelberg, 2006, pp. 85–95. DOI: 10.1007/11889762_8.

[92] Zhun Fan et al. *Automatic Pavement Crack Detection Based on Structured Prediction with the Convolutional Neural Network*. Feb. 2018. arXiv: 1802.02208 [cs].

[93] Martín Abadi et al. *TensorFlow: Large-scale Machine Learning on Heterogeneous Systems*. 2015.

[94] Johannes Schindelin et al. "Fiji: An Open-Source Platform for Biological-Image Analysis". In: *Nature Methods* 9.7 (July 2012), pp. 676–682. DOI: 10.1038/nmeth.2019.

[95] Stéfan van der Walt et al. "Scikit-Image: Image Processing in Python". In: *PeerJ* 2 (June 2014), e453. DOI: 10.7717/peerj.453.

[96] Martin Hunt. *Jupyter Lab*. nanoHUB. 2018. DOI: 10.4231/D3F766898.

[97] Thomas A Caswell et al. *Matplotlib/Matplotlib: REL: V3.2.1*. Zenodo. Mar. 2020. DOI: 10.5281/ZENODO.3714460.

[98] Travis E Oliphant. *A Guide to NumPy*. Vol. 1. Trelgol Publishing USA, 2006.

[99] Hugo Van Kemenade et al. *Python-Pillow/Pillow 7.1.2*. Zenodo. Apr. 2020. DOI: 10.5281/ZENODO.3766443.

[100] Nicholas Sofroniew et al. *Napari/Napari: 0.3.3*. Zenodo. May 2020. DOI: 10.5281/ZENODO.3555620.

[101] Geo Davis et al. "Laser Ultrasonic Inspection of Additive Manufactured Components". In: *The International Journal of Advanced Manufacturing Technology* 102.5-8 (June 2019), pp. 2571–2579. DOI: 10.1007/s00170-018-3046-y.

[102] Feixiang Yan, Hong Zhang, and C. Ronald Kube. "A Multistage Adaptive Thresholding Method". In: *Pattern Recognition Letters* 26.8 (June 2005), pp. 1183–1191. DOI: 10.1016/j.patrec.2004.11.003.

[103] Tomás Gómez Álvarez-Arenas and Jorge Camacho. "Air-Coupled and Resonant Pulse-Echo Ultrasonic Technique". In: *Sensors* 19.10 (May 2019), p. 2221. DOI: 10.3390/s19102221.